

## Using 3.4- $\mu$ m Variability towards White Dwarfs as a Signpost of Remnant Planetary Systems

JOSEPH A. GUIDRY , \* J. J. HERMES  KISHALAY DE , † LOU BAYA OULD ROUIS  BRISON B. EWING ,  
 AND B. C. KAISER 

<sup>1</sup>Department of Astronomy, Boston University, Boston, MA 02215, USA

<sup>2</sup>Institute for Astrophysical Research, Boston University, Boston, MA 02215, USA

<sup>3</sup>MIT-Kavli Institute for Astrophysics and Space Research, Cambridge, MA 02139, USA

<sup>4</sup>Department of Physics and Astronomy, University of North Carolina at Chapel Hill, Chapel Hill, NC 27599, USA

(Received April 18, 2024; Revised June 21, 2024; Accepted June 24, 2024)

Submitted to ApJ

### ABSTRACT

Roughly 2% of white dwarfs harbor planetary debris disks detectable via infrared excesses, but only a few percent of these disks show a gaseous component, distinguished by their double-peaked emission at the near-infrared calcium triplet. Previous studies found most debris disks around white dwarfs are variable at 3.4 and 4.5  $\mu$ m, but they analyzed only a few of the now 21 published disks showing calcium emission. To test if most published calcium emission disks exhibit large-amplitude stochastic variability in the near-infrared, we use light curves generated from the unWISE images at 3.4  $\mu$ m that are corrected for proper motion to characterize the near-infrared variability of these disks against samples of disks without calcium emission, highly variable cataclysmic variables, and 3215 isolated white dwarfs. We find most calcium emission disks are extremely variable: 6/11 with sufficient signal-to-noise show high-amplitude variability in their 3.4- $\mu$ m light curves. These results lend further credence to the notion that disks showing gaseous debris in emission are the most collisionally active. Under the assumption that 3.4- $\mu$ m variability is characteristic of white dwarfs with dusty debris disks, we generate a catalog of 104 high-confidence near-infrared variable white dwarfs, 84 of which are published as variable for the first time. We do near-infrared spectroscopic follow-up of seven new candidate 3.4- $\mu$ m variables, confirming at least one new remnant planetary system, and posit that empirical near-infrared variability can be a discovery engine for debris disks showing gaseous emission.

**Keywords:** White dwarf stars (1799) — Debris disks (363) — Variable stars (1761) — Exoplanet systems (484) — Infrared excess (788) — Transient detection (1957) — Collisional processes (2286)

### 1. INTRODUCTION

More than 30% of all white dwarf stars are likely accreting close-in circumstellar debris disks (Zuckerman et al. 2003, 2010; Koester et al. 2014; Ould Rouis et al. 2024) composed of planetary bodies disrupted by tidal forces (Jura 2003). These debris disks are most commonly inferred from the observation of metals polluting the otherwise pure hydrogen or pure helium white dwarf photosphere. Mass fractions of these pollutants

are largely consistent with a rocky composition similar to bulk Earth (Xu et al. 2014; Xu & Bonsor 2021). Metal pollution is interpreted as a signpost for the presence of a remnant planetary system bound to the white dwarf (see Veras 2021, and references therein).

Dust liberated from the disruption of these rocky bodies via ensuing grind-down from planetesimal collisions (e.g., Malamud et al. 2021; Brouwers et al. 2022) can be detected as infrared emission in excess to the white dwarf photosphere. Roughly 2% of white dwarfs exhibit a detectable infrared excesses indicative of warm, dusty debris disks (Rocchetto et al. 2015; Wilson et al. 2019; Rebassa-Mansergas et al. 2019). This smaller detection rate could be a consequence of needing near-face-on viewing geometries if these disks tend to be flat. Regardless, all white dwarfs with dusty disks show ph-

Corresponding author: Joseph A. Guidry  
 jaguidry@bu.edu

\* NSF Graduate Research Fellow

† NASA Einstein Fellow

tospheric metal pollution (see Farihi 2016 and references therein). These infrared excesses peak at mid-infrared wavelengths ( $\gtrsim 5 \mu\text{m}$ ) and are challenging to observe from the ground; white dwarfs with infrared excesses peaking in the near-infrared ( $\lesssim 5 \mu\text{m}$ ) are more likely to host to an unresolved, cool stellar or brown dwarf companion (e.g., Farihi et al. 2005; Girven et al. 2011; Dennihy et al. 2020b).

At the innermost radii of the debris disk, the temperatures should be sufficient to sublimate the debris into gaseous states. This gas can be viewed in absorption (e.g., Debes et al. 2012; Xu et al. 2016; Steele et al. 2021) and as broad, double-peaked emission, mainly at the calcium triplet (Gänsicke et al. 2006, 2007, 2008; Gänsicke 2011; Farihi et al. 2012; Melis et al. 2012; Wilson et al. 2014; Melis et al. 2020; Dennihy et al. 2020b; Gentile Fusillo et al. 2021a). The latter class of “gaseous” debris disk systems are observationally rare: Manser et al. (2020) calculate the occurrence rate of white dwarfs showing emission at the Ca II triplet to be  $\approx 0.1\%$ . Notably, all 21 published gas disk systems are metal polluted (Gentile Fusillo et al. 2021a) and most show infrared excesses (see Farihi 2016 and references therein; Gentile Fusillo et al. 2021a). Many of the white dwarfs hosting gaseous disks show heavily polluted photospheres, though this circumstellar gas so far does not appear to enhance accretion rates via drag effects (Rogers et al. 2024a). This class of disks showing gaseous calcium is distinct from cases like that of WD J0914+1914, which harbors a gas-only, dustless disk fueled by the evaporation of a volatile rich atmosphere of a giant planet, and not a disrupted rocky body (Gänsicke et al. 2019).

Throughout the remainder of this paper we adopt a nomenclature of disks “showing calcium (Ca II) gas in emission” and “non-calcium emission (non-Ca II)” disks to distinguish the dusty debris disks that have previously been observed to show a gaseous component in emission at the calcium II triplet in the near-infrared, since gaseous and dusty debris are believed to coexist in all of these planetary debris disks.

Among a sample of 35 non-Ca II dusty white dwarfs observed by the Wide-field Infrared Survey Explorer (WISE), Swan et al. (2019) found that the majority exhibit significant photometric variability in the near-infrared at  $3.4 \mu\text{m}$ . Ensemble variability was again observed by Swan et al. (2020) among a sample of over 40 white dwarf debris disks with Spitzer at  $3.4 \mu\text{m}$  and  $4.5 \mu\text{m}$ . Within this sample, a few Ca II gas disk systems have shown exaggerated, high-amplitude variability (Swan et al. 2020). This includes factor-of-two brightenings in the near-infrared seen towards WD 0145+234 (Wang et al. 2019, Figure 1 Panel a), interpreted as an expansion of the emitting area of the dust disk due to collisions (Swan et al. 2021), which in turn should liberate gas. It also includes dimmings, like those observed with Spitzer towards WD J0959–0200

(Xu & Jura 2014), SDSS J1228+1040 (Xu et al. 2018), and GD 56 (Farihi et al. 2018). Rogers et al. (2020) did not observe ensemble variability in the  $J$ -,  $H$ -, and  $K$ -bands over a three-year baseline among dusty white dwarfs.

We explore here the  $3.4\text{-}\mu\text{m}$  variability of all 21 published Ca II gas disk systems in ensemble for the first time. We aim to test whether they exhibit stochastic variability when bright enough to be confidently detected in WISE. We generate light curves using a new aperture photometry pipeline that corrects for the proper motions of targets as it operates on the unWISE images from the NEOWISE era (2013–2023). We are motivated to test if empirical  $3.4\text{-}\mu\text{m}$  variability can be used as an engine for discovering more disks showing Ca II emission around white dwarfs.

In Section 2 we describe our light curve generation pipeline and follow-up observations. In Section 3 we detail our variability ranking and validation method. In Section 4 we report our catalog of  $3.4\text{-}\mu\text{m}$  variables and characterize the Ca II disks relative to non-Ca II disks. We end by discussing the consequences of our work in Section 5. Our catalog of  $3.4\text{-}\mu\text{m}$  variables is published in Appendix A.

## 2. OBSERVATIONS

### 2.1. New unWISE Light Curve Extractions

Our study utilizes images from the unWISE individual-image catalog<sup>1</sup> captured by the all-sky survey of the Wide-field Infrared Survey Explorer (WISE, Wright et al. 2010), including the initial cryogenic mission and the ongoing NEOWISE mission (Mainzer et al. 2011, 2014). The unWISE catalog features coadded images of typically  $12 \times 7.7\text{s}$  exposures (Meisner et al. 2018), boosting photometry reliability to magnitudes of  $W1 \sim 18\text{ mag}$  (Schlafly et al. 2019). The images are  $2048 \times 2048$  pixels at a scale of  $2.75''$  per pixel (Lang 2014), although the typical image resolution from the PSF is roughly  $6.1''$  and  $6.3''$  in the  $W1$  ( $3.4 \mu\text{m}$ ) and  $W2$  ( $4.6 \mu\text{m}$ ) channels, respectively. For a thorough description of the unWISE catalog see Schlafly et al. (2019), and for a review of the image processing and generation see Lang (2014) and Meisner et al. (2017a,b). We use the unWISE images from the 2023 NEOWISE Data Release.

Our pipeline operates on the single coadds for each epoch, treating the  $W1$  and  $W2$  images separately. Another version of this pipeline uses difference imaging for transient work in WISE (Tran et al. 2024; Masterson et al. 2024). Here instead we perform simple aperture photometry, using a fixed circular 2-pixel-radius aperture (equivalently  $5.5''$ ) centered on the coordinates of the target to match the WISE PSF. We also draw an

<sup>1</sup> <https://catalog.unwise.me/catalogs.html>

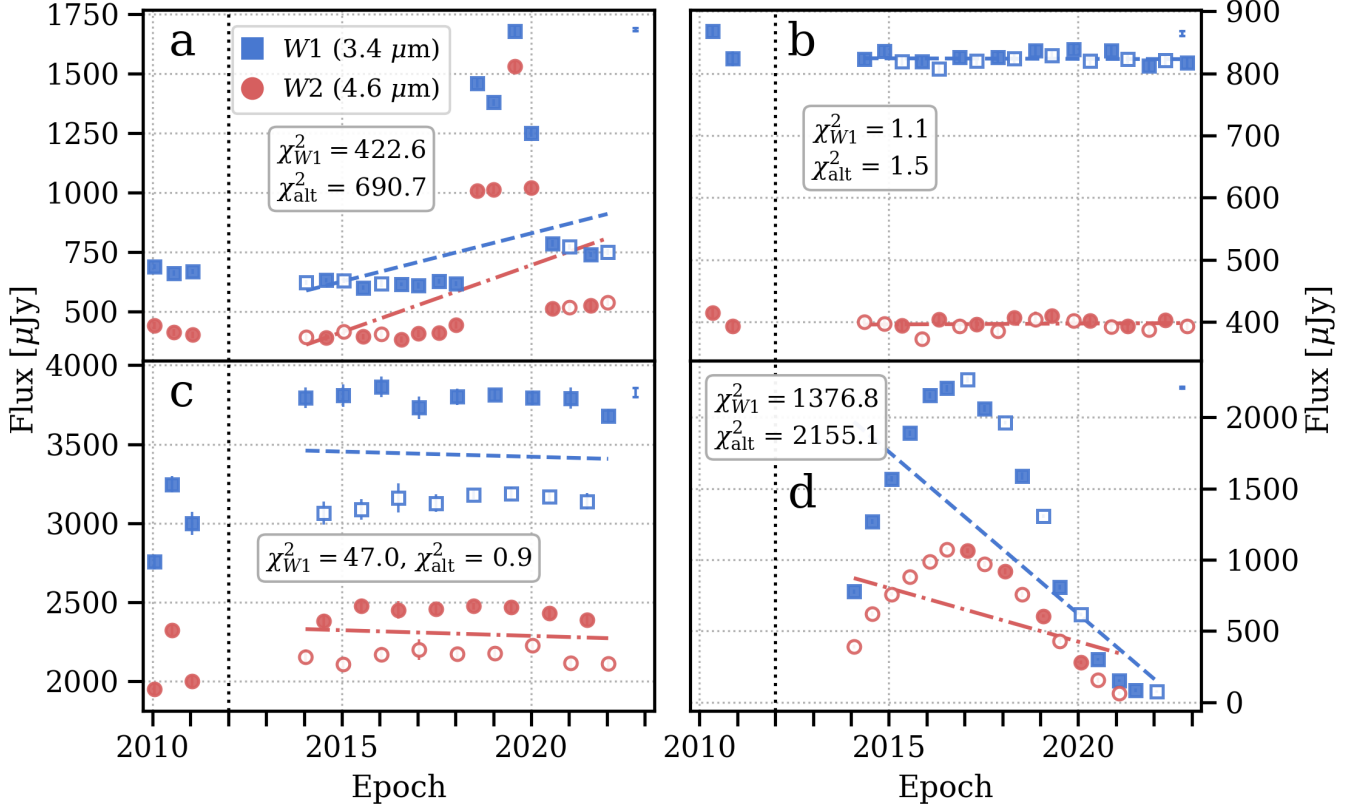


**Figure 1.** WISE light curves for W1 (3.4  $\mu$ m, blue squares) and W2 (4.6  $\mu$ m, red circles) representing the four most common trends seen in our sample. (a) Significant, stochastic variability, such as the outbursting Ca II gas disk towards the previously studied WD 0145+234 (Swan et al. 2021). (b) A flat light curve representing the expectation for an isolated, unchanging white dwarf (LAWD 52). (c) A light curve showing a strong alternating pattern in both the W1 and W2 bands caused by the different scanning angles of the PSF from each 6-month WISE observing season, which tends to be exacerbated when there are nearby stars to the target (PG 1411+219). The solid- and open-faced points indicate the two clusters used to calculate  $\chi^2_{\text{alt}}$  (see text). (d) A secular brightening or dimming trend caused by the proper motion of the white dwarf (GJ 3770) moving into (or away from) another star. The dotted black lines at 2012 demarcate the transition from cryogenic to NEOWISE mission data; we only analyze the NEOWISE epochs for our variability rankings. Blue dashed and red dashed-dotted lines show the fits used to calculate  $\chi^2_{W1}$  and  $\chi^2_{W2}$ , respectively (see Section 3 for definitions of the annotated  $\chi^2$  values). Uncertainties are shown but are generally smaller than each symbol. The average W1 uncertainties are plotted in the upper right corner of each panel.

annulus with an inner radius of 5 pixels and width of 3 pixels for background subtraction. Importantly, we propagate the coordinates of each target using the Gaia DR3 measured right ascension, declination, and proper motions to the epoch of the WISE observation, rather than doing source detection from epoch-to-epoch like unTimely (Meisner et al. 2023). Representative light curves are shown in Figure 1. The proper motions of field stars are not included, nor are the parallaxes of any sources. We also generate light curves extracted by PSF photometry on the unWISE images using the same procedures.

We estimate uncertainties on the photometry using the uncertainty images provided by WISE and further processed by unWISE that map uncertainties to the pixel-level (Lang 2014). Objects varying on timescales of seconds generate greater uncertainties due to the larger

image-to-image deviations. A full detailed account of this pipeline will be presented in a forthcoming publication, K. De et al. (in prep).

## 2.2. Input White Dwarf Catalog

We construct a sample for our study that includes all white dwarfs currently known to harbor gaseous debris disks and various control samples to assess the variability of the Ca II gas disks. The 21 Ca II gas disk systems are sourced from Table 3 of Gentile Fusillo et al. (2021a). Our first control sample is one of 45 white dwarfs with known infrared excesses due to dusty debris disks that have not shown calcium triplet emission: 28 from the Montreal White Dwarf Database (Dufour et al. 2017), seven systems not in MWDD from Rogers et al. (2020), and 11 more unique systems from Wang et al. (2023). We would go on to find two additional known dusty

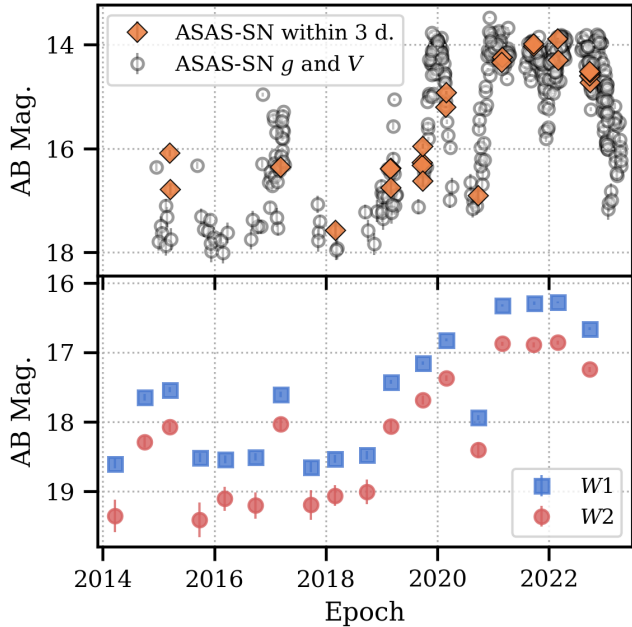


**Figure 2. Top:** ASAS-SN light curve (Shappee et al. 2014; Kochanek et al. 2017; Hart et al. 2023) of the cataclysmic variable KR Aur (Gaia DR3 3436435910858051200). Observations shown as orange diamonds were taken to within 3 days of the WISE epochs, while the remaining open-faced points show the full  $g$ - and  $V$ -band light curve. **Bottom:** Our WISE light curve of KR Aur showing a correlation between the optical and near-infrared variability.

disks in the Gaia-catWISE input described below after ranking all systems by their variability: KPD 0420+5203 (Gaia DR3 271992414775824640) (Hoard et al. 2013; Barber et al. 2016) and MCT 0420–7310 (Gaia DR3 4653404070862114176) (Hoard et al. 2013; Dennihy et al. 2017), yielding an input of 47 objects.

Our second control is a sample of 14 known cataclysmic variables (CVs) taken from the American Association of Variable Star Observers<sup>2</sup> with Gaia G-band magnitudes of  $13 \leq G \leq 18$  mag, three recently discovered polars (Guidry et al. 2021; Rodriguez et al. 2023a) and one AM CVn (Rodriguez et al. 2023b) from the Zwicky Transient Facility. The CV sub-sample is meant to be a test to the pipeline, as CVs are known to show both optical and IR outbursts (e.g., Petrosky et al. 2021); correlated optical and infrared variability of KR Aur, a known CV, is shown in Figure 2.

We build a third sample from a cross-match between the Gaia eDR3 catalog of white dwarfs (Gentile Fusillo et al. 2021b) and the catWISE catalog of WISE-detected sources (Eisenhardt et al. 2020). We intend to search for highly variable white dwarfs within this sample to

identify candidate gas disks, as well as contextualize the variability of the known debris disks against that of isolated white dwarfs. We first cut the Gaia white dwarf catalog to 100 pc and impose  $P_{WD} > 0.75$  to define a sample of high-confidence, isolated white dwarfs, eliminating most binary sources like CVs or unresolved WD+MS, post-common-envelope binaries. We require all sources be brighter than  $G_{RP} < 17.0$  mag, and cross-match with catWISE, requiring the  $W_2$  detections to have a signal-to-noise greater than 5.0 and the  $W_1$  magnitudes be within 1.5 mag of the Gaia  $RP$  magnitude. This yields a final source catalog of 3215 white dwarfs, including multiple duplicates from the above Ca II and non-Ca II disks and CV sub-samples. Aggregating all these samples, we build an input catalog of 3299 white dwarfs.

### 2.3. Near-Infrared Spectroscopic Follow-up

#### 2.3.1. LDT+DeVenY

Our primary motivation for ranking white dwarfs by their WISE variability is to build a catalog of candidate remnant planetary systems, especially those with the highest potential to host collisionally active debris disks. We began a preliminary follow-up campaign to test if these candidates show emission at the calcium triplet using the DeVenY Spectrograph (Bida et al. 2014) at the 4.3-m Lowell Discovery Telescope (LDT) at Happy Jack, Arizona, USA.

For our LDT+DeVenY observations we use a 1.0'' slit paired with the DV8 grating (831 line/mm) centered at a blaze wavelength of 8000 Å with the GG 570 order-blocking filter, yielding a resolution of roughly 0.8 Å across 7200–8800 Å. We publish observations here from 2023 June 20 and 2024 February 5. We provide a log of our LDT+DeVenY observations in Table 5 in Appendix B.

We reduced our spectra using the PypeIt reduction pipeline (Prochaska et al. 2020), performing a telluric correction directly on our observations using a third-order polynomial model to estimate the continuum.

#### 2.3.2. SOAR+Goodman Follow-up

We also followed up some of our southern candidates using the red camera of the Goodman Spectrograph (Clemens et al. 2004) mounted on the 4.1-m Southern Astrophysical Research Telescope (SOAR) at Cerro Pachón, Chile on 2023 August 13 and 2023 August 18. Building on the observations of Ca II gas disks done by Dennihy et al. (2018, 2020b), we use the 1200 line/mm grating with the 1.0'' slit and GG495 order-blocking filter, giving us spectral coverage from roughly 7570–8750 Å with a resolution of roughly 0.6 Å. Alongside the LDT+DeVenY spectra, a log of our SOAR observations can be found in Table 5 in Appendix B.

We also reduce our SOAR spectra using PypeIt, again performing a telluric correction on our spectra anchored to a third-order polynomial over the region observed.

<sup>2</sup> <https://targettool.aavso.org/TargetTool/default/index>

### 3. VARIABILITY DETECTION AND VALIDATION

We first process each WISE light curve through quality filtering before assessing it for variability, handling the  $W1$  and  $W2$  observations independently. We reject erroneous measurements (zero flux detections) and require both the  $W1$  and  $W2$  flux uncertainties be  $> 1 \mu\text{Jy}$ . We further perform a  $3\sigma$  clip to the flux uncertainties to exclude spuriously small values that would skew a  $\chi^2$  calculation. Finally we require the signal-to-noise ratio of each epoch be  $S/\text{N} > 3.0$ . We then convert the WISE Vega magnitudes to fluxes in Janskys using the published conversions:  $F_{\nu,0,W1} = 309.540 \text{ Jy}$ ,  $F_{\nu,0,W2} = 171.787 \text{ Jy}$  (Jarrett et al. 2011; Wright et al. 2010). All analysis of the WISE light curves is hereafter conducted in flux space.

Presuming an isolated white dwarf should be constant in infrared flux, we assess the degree of variability for each object by the goodness of linear (first-order polynomial) fits to each light curve. Keeping the  $W1$  and  $W2$  light curves independent, we fit lines to the NEOWISE-only (2013 – 2023) portion of each light curve, allowing the slopes and offsets to vary. Calibrations for the first few cryogenic epochs collected from 2009 – 2011 can cause flux offsets from the NEOWISE data (Meisner et al. 2017a). For every object we record the reduced  $\chi^2$  of each fit to each band, hereafter referred to as  $\chi^2_{W1}$  and  $\chi^2_{W2}$ , respectively. We do the same to for an additional series of linear fits where the slope is fixed to be zero. We designate these “flat” line fits to the  $W1$  light curves as  $\chi^2_{\text{flat}}$ .

A common artifact seen in the light curves from WISE is an alternating set of fluxes due to the rotation of the point-spread function (PSF) from the different scanning angles of the spacecraft from epoch-to-epoch (Eisenhardt et al. 2020). Panel c of Figure 1 shows an example of this variation, alternating with the typical source revisit timescale of roughly 6 months. This causes the source to exhibit both large  $\chi^2_{W1}$  and  $\chi^2_{\text{flat}}$  while not necessarily being intrinsically astrophysically variable.

We define a second goodness-of-fit metric that analyzes each “high” and “low” season independently. We use a one-dimensional  $k$ -means clustering algorithm<sup>3</sup> to sort each light curve temporally, dividing the timestamps by the median separation of the whole light curve, taking the modulo of twice that median revisit timescale to convert the light curve points into two clusters in phase space. The cluster with the higher average flux is classified as the “high” cluster and the other the “low.” We fit an additional pair of lines to each cluster for each filter. We calculate an effective reduced  $\chi^2$  for these “high-and-low” seasons as  $\chi^2_{\text{alt}} = (\chi^2_{\text{high}} + \chi^2_{\text{low}})/\sqrt{2}$ . The comparison of  $\chi^2_{\text{alt}} - \chi^2_{W1}$  is shown in the top panel of Figure 3. We de-prioritize objects with  $\chi^2_{\text{alt}} - \chi^2_{W1} < 0$ ,

as they are more likely to have flux changes due to the WISE scanning angle rather than some intrinsic variability, as exhibited in Panel c of Figure 1.

We further attempted to quantify contamination by comparing the flux of our target in the Gaia  $G_{\text{RP}}$  bandpass to the sum of all flux from objects within a  $30''$  radius of the target. We find that the visually classified contaminated objects suffer when the nearby sources sum to  $> 1.415 \times$  the  $G_{\text{RP}}$  flux of the target. We selected the factor-of-1.415 threshold from a 1-d  $k$ -means sorting of the total  $G_{\text{RP}}$  fluxes from the  $30''$  cones into two clusters. The centroid of the cluster of lowest fluxes was 1.415. The top panel of Figure 3 shows objects marked as “likely crowded” based on this analysis, and we discontinue consideration of these crowded objects. We refer to this parameter as “ $G_{\text{RP}}$  Excess” in the tables in Appendix A.

Our quality filtering removes 883 likely alternating sources (those with  $\chi^2_{\text{alt}} - \chi^2_{W1} < 0$ ) and removes all likely crowded sources (827 total) through our cut on the Gaia  $G_{\text{RP}}$  fluxes, leaving 1590 objects in total, or about 48% of the original sample. Although non-Gaussian, if these 1590 objects were normally distributed in  $\chi^2_{W1}$ -space, the  $3\sigma$  limit would be  $\chi^2_{W1} = 2.3$ .

We build a catalog variable white dwarfs as seen by WISE by ranking our sample by  $\chi^2_{W1}$ , since signal-to-noise ratio is on average higher in the  $W1$  band. We report  $\chi^2_{W2}$  values in the tables of Appendix A, but do not incorporate them into our variability analysis. Having removed likely alternating and crowded sources, we impose a third cut to yield a final sample, keeping sources only with a  $\chi^2_{W1} > 2.0$  or  $\chi^2_{\text{flat}} > 2.0$  to include sources that are showing potentially real, secular variations. Hereafter we abbreviate this ambiguity to simply  $\chi^2$ . A cut at  $\chi^2 > 2.0$  keeps the top 89th percentile of the “non-alternating” and “uncrowded” sample. This final catalog, shown in the bottom panel of Figure 3 and published in Table 2, contains a total of 163 unique sources.

We assess the fidelity of the unWISE images for all these candidate variables and special samples (all the known gas disks, known infrared excess systems, known CVs). The unWISE images have a relatively large ( $> 6''$ ) PSF full-width-at-half-maximum (Wright et al. 2010), making source contamination another major issue (Dennihy et al. 2020a). We visually vetted our catalog of variables using the WISE View tool<sup>4</sup> to inspect each unWISE image of each candidate centered on its J2000 coordinates. We look in particular for the proper motion of targets bringing them towards or away from a nearby field source in a manner correlated with the computed light curve. We mark these objects as contaminated in Figure 3 and Table 2. Panel d of Figure 1 shows an example of a secular brightening of a white dwarf mov-

<sup>3</sup> <https://github.com/dstein64/kmeans1d>

<sup>4</sup> <http://byw.tools/wiseview>

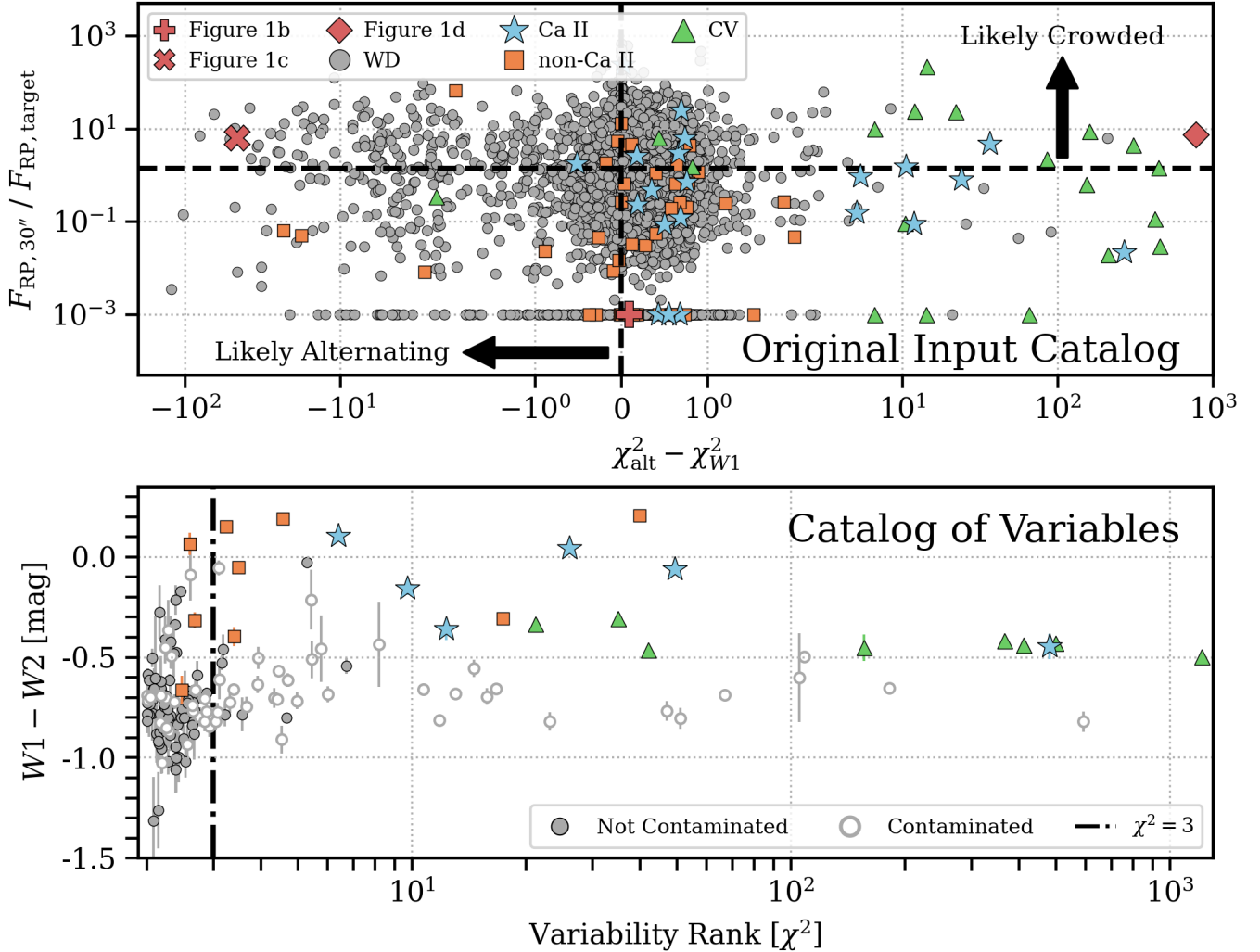


**Figure 3. Top:** Excess Gaia *RP* flux vs. the difference between the “alternating”  $\chi^2$  (see Panel c of Figure 1) and the  $\chi^2_{W1}$  fits. Sources with  $\chi^2_{\text{alt}} - \chi^2_{W1} < 0$  are likely to have high  $\chi^2_{W1}$  caused by the alternating pattern due to the biannual variation in the WISE PSF scanning angle, rather than astrophysical variability. Sources with 1.415 times more flux in the Gaia *RP* channel in a  $30''$  cone than their own flux are frequently found in crowded fields, leading to false-positive variability detections due to source crowding of the large WISE PSF and proper motions like that in Panel d of Figure 1 due to proper motions. We inflate y-axis values by  $10^{-3}$  so that sources with zero nearby flux are on-axis. **Bottom:** Our catalog of 163 3.4- $\mu\text{m}$  variables ranked by variability. Catalog inclusion requires  $\chi^2_{\text{alt}} - \chi^2_{W1} > 0$ ,  $G_{RP}$  excess flux  $< 1.415 \times$  the target flux, and  $\chi^2_{W1}$  or  $\chi^2_{\text{flat}} > 2.0$  (see text). The x-axis values are the maximum value of  $\chi^2_{W1}$  or  $\chi^2_{\text{flat}}$  for each target. Objects with strong apparent contamination from visual inspection with WISE View and/or still show a seasonal alternating pattern (see the Flag column in Table 2) are shown as open-faced (only found for Gaia-catWISE white dwarfs). The vertical dash-dotted line at  $\chi^2 = 3$  marks our definition for high-amplitude variability. In all panels, we distinguish known disks with calcium emission as cyan stars, white dwarfs with dusty disks without calcium emission as orange squares, and known CVs as green triangles.

ing into a bright background source. We also denote objects that still show a seasonal alternating pattern as contaminated in Figure 3 and Table 2.

#### 4. VARIABILITY ANALYSIS

Here we report the results of our variability ranking. In Section 4.1 we breakdown our catalog of 3.4- $\mu\text{m}$  vari-

ables. We reserve Section 4.2 for analyzing the Ca II and non-Ca II debris disk systems in our catalog. We showcase the results of our near-infrared spectroscopic follow-up in Section 4.3.

##### 4.1. Catalog of 3.4- $\mu\text{m}$ Variables

We build our catalog of candidate variables by selecting sources with either  $\chi^2_{W1} > 2.0$  or  $\chi^2_{\text{flat}} > 2.0$  (top 11% most variable), which includes 163 unique white

**Table 1.** Demographic Evolution of our Sample from the Original Input to our Catalog of Variables.

Sample	Original Input	Pass Filtering	S/N > 10	Variable ( $\chi^2 > 2$ )	Uncontaminated	Highly Variable ( $\chi^2 > 3$ )
Disks with Ca II Emission	21	13	11	6	6	6
Disks without Ca II Emission	47	29	17	9	9	6
Cataclysmic Variables	18	8	8	8	8	8
Gaia-catWISE	3213	1540	900	140	81	10
Total	3299	1590	936	163	104	30

NOTE—Description of columns: From left to right we record the original number of our input, the amount that pass our quality filtering, the amount that have signal-to-noise>10 in our  $W_1$  light curves, the amount we find variable ( $\chi^2 > 2$ ), the amount of variables that do not appear contaminated upon closer examination, and finally the amount within our catalog that show high-amplitude variability ( $\chi^2 > 3$ ).

dwarfs. We break down in Table 1 the demographics of our catalog relative to the original inputs. Our catalog is tabulated in full in Table 2. Among these 163 we find 104 uncontaminated sources that we believe to be high-confidence variables at 3.4  $\mu$ m, 84 of which are published as near-infrared variables for the first time based on our literature search.

The known CVs are by far the most variable in our catalog: all eight are within the top 90th or higher percentile of our variable catalog, and all have  $\chi^2 > 20$ . None of these eight show evidence for having contaminated photometry. The Ca II gas disk systems also show exceptionally large-amplitude variability. We defer characterization of their variability and that of the dusty disks to Section 4.2.

We search for optical variability within our catalog to offer some characterization. We report the EXCESS\_FLUX\_FACTOR (abbreviated as EFF in the tables of Appendix A) for all these 3.4- $\mu$ m candidate variables in Table 2, a metric that reliably quantifies empirical variability from Gaia photometry (Gentile Fusillo et al. 2021b). We also use astroquery (Ginsburg et al. 2019) to download any 20-second- and 2-min-cadence PDC-SAP light curves captured by the Transiting Exoplanet Survey Satellite (TESS, Ricker et al. 2015) of our candidate variables. We report the maximum period and associated amplitude from the 2-min light curves if it is significant to a false-alarm threshold of 0.1% in Table 2. We use the tool TESS.localize to confirm with >99% likelihood that the signal is coming from our often-crowded white dwarfs (Higgins & Bell 2023).

Beyond the eight previously known CVs, we recover 10 additional known variable white dwarfs in our final sample. This includes the known AM CVn G 61–29 (Gaia DR3 3938156295111047680, Nather et al. 1981), eight pulsating white dwarfs (see Table 2), and one spotted magnetic white dwarf (WD 1953–011, Gaia DR3 4235280071072332672, Brinkworth et al. 2005; Valyavin et al. 2011). Like the CV KR Aur shown in Figure 2, these recoveries further confirm that our method returns real astrophysical variables.

At optical wavelengths, 34 of the 163 sources in our catalog are flagged in Gaia DR3 as photometrically vari-

able (Eyer et al. 2023). Within these 34 are all eight CVs, one infrared excess system that is a known ZZ Ceti (Gaia DR3 1641326979142898048), and the gas disk system WD 0145+234. While WD 0145+234 has both a negative VARINDEX (Guidry et al. 2021) and an EXCESS\_FLUX\_ERROR<1 (Gentile Fusillo et al. 2021b), suggesting it is not variable over long baselines, the flagging by Eyer et al. (2023) indicates it may show optical variability on some timescale.

Most of the white dwarfs in our catalog of 3.4- $\mu$ m variables do not show coherent periodic variability in the optical as seen by TESS. We find only 13 of our 163 sources in our catalog to show a significant period intrinsic to white dwarf as determined by TESS.localize. We stress these fractions cannot be compared exactly, given the differences in cadence and baselines. Seven of these 13 are known pulsating white dwarfs, including KX Dra (Gaia DR3 1641326979142898048, Vauclair et al. 2000) and WD 1150–153 (Gaia DR3 3571559292842744960, Gianninas et al. 2006), a known non-Ca II gas debris disk, and four are known CVs. One of these 13 objects is Gaia DR3 3150770626615542784, which shows a significant periodicity at 200.31 s at an amplitude of 0.69% over its 20-second light curves in Sectors 44 – 46. Vincent et al. (2020) targeted this object because of its position in the ZZ Ceti instability but did not observe it to vary. We believe these TESS observations confirm it as a new pulsating white dwarf. Three of these 13 appear to show contaminated WISE light curves (see below). We highlight all of these TESS variables in Table 2 by including the period and associated amplitude of variability. Lastly, we reject that WD 0420+520 is a candidate eclipsing binary (Prša et al. 2022). Our TESS.localize analysis points towards Gaia DR3 271992483495298688 as the source of the apparent variability.

Based on visual inspection of the unWISE images using WISE View, we flag 35 of the 163 variables in our catalog as possibly contaminated by a nearby infrared source (21%). These 35 (which are made up of sources only from our Gaia-catWISE crossmatch and includes no debris disk systems) appear to show variability correlated with the proper motion of the white dwarf or a nearby field star as seen in WISE View. We still publish

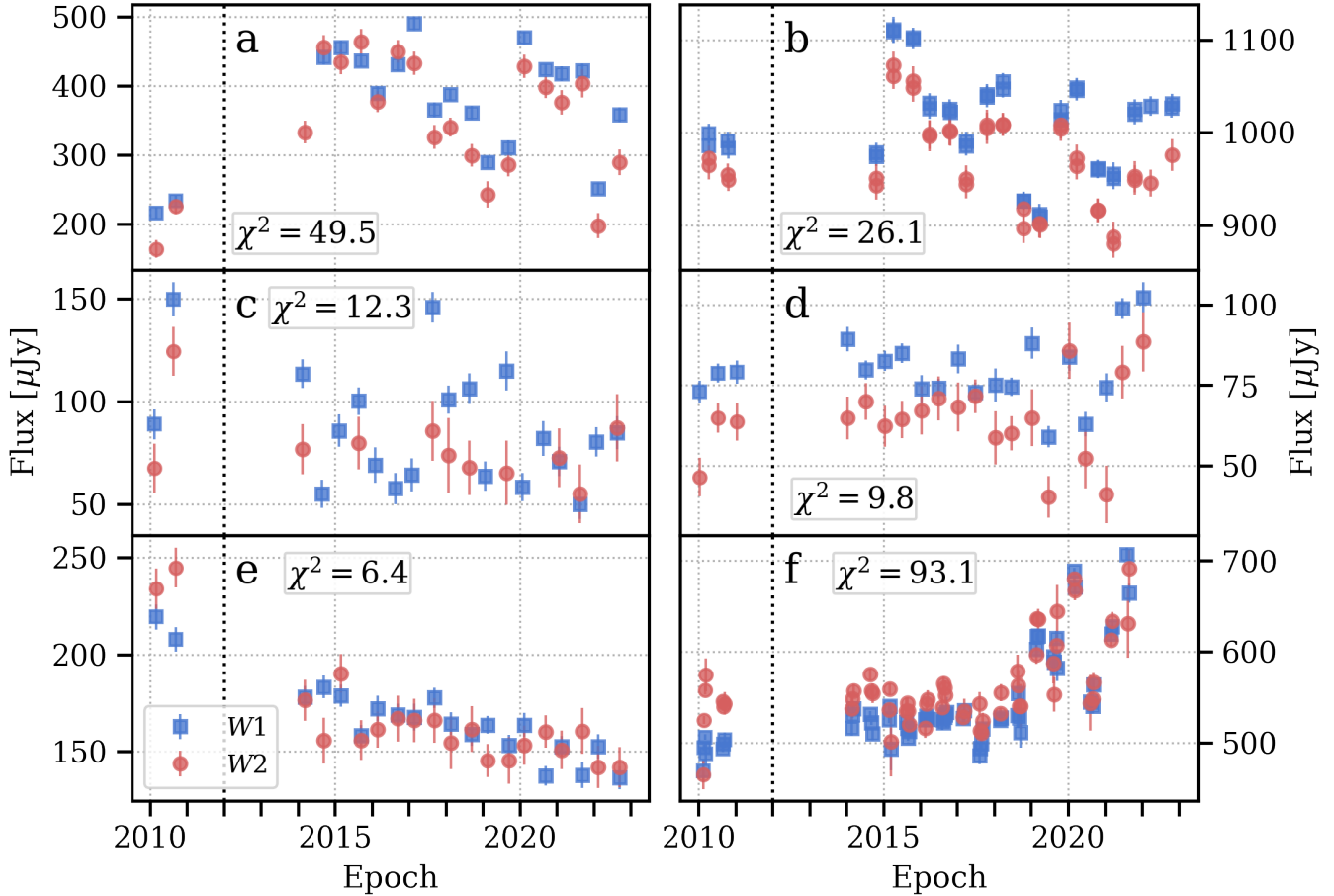


**Figure 4.** WISE light curves of the white dwarfs with known Ca II gas disks in our variability catalog (all discovered in Melis et al. 2020, unless noted otherwise): a LAMOST J0510+2315, b WD 0842+572, c SDSS J0347+1624, d WD 1622+587 (and Dennihy et al. 2020b), e WD J0529–3401 (Gentile Fusillo et al. 2021a). Each shows extreme variability: all have  $\chi^2 > 6$  and peak-to-peak flux changes in  $W1 > 20\%$ . None of these systems have had their infrared light curves characterized before. We show Gaia J0611–6931 (and Dennihy et al. 2020b) in Panel F. Despite its exclusion from our catalog for possible crowding, we do not see evidence for obvious contamination in WISE View. Its disk may be undergoing a real brightening. WD 0145+234 (Figure 1 Panel A) is the only Ca II gas disk in our variable catalog not shown here.

these “contaminated” objects as candidate 3.4- $\mu$ m variables, but flag them in Table 2 due to the subjectivity of this exercise.

Finally, we note our catalog of variables is still subject to further crowding and contamination due to the large WISE PSF. At least 31 of 163 objects still probably show an alternating pattern in their light curves (seven of which also have contaminated photometry). This is likely in part due to our clustering and sorting technique sometimes failing to identify the “high” and “low” seasons generated by the alternating PSF scanning angle of WISE. This technique particularly fails to filter out potentially false-positive variability due to multiple observations being taken during the same epoch. For example, WD 0028–474 (Gaia DR3 4978793541987799040) and WD 2118–388 (Gaia DR3 6583325635088476544) have two flux measurements per epoch for most epochs. In each case, the two concurrent measurements lie on

two distinct flux baselines, forming “high” and “low” tracks at all epochs, rather than alternating from epoch-to-epoch like in Panel b of Figure 1. Neither object shows evidence for rapid variability in TESS. It is unclear what is responsible for the apparent variability seen towards these two systems. Subsequent NEOWISE observing fields do tend to overlap by about 3' at all ecliptic latitudes (Meisner et al. 2019), generating multiple observations at the same epoch with possible differences in flux due to the PSF scanning angle varying as the spacecraft scans from field-to-field (Schlafly et al. 2019). These two objects are not located at extreme ecliptic latitudes (both lie between  $-55^\circ < \beta < -35^\circ$ ). Both the non-contaminated and contaminated subsets of our catalog of variables appear to be distributed across all ecliptic latitudes.

In the tables in the Appendix we include the `score` statistic calculated in the Gaia DR3

`allwise_neighbourhood`<sup>5</sup> table (Marrese et al. 2017, 2019, 2022) as an additional Figure of Merit (FoM) for users to vet the sources in our catalog. We do not use the FoM to flag objects due to its incompleteness (41/163 objects in our catalog are not included in the Gaia-AllWISE neighborhood crossmatch analysis). Dennihy et al. (2020a) found white dwarf targets with  $S/N > 10$  in  $W1$  and  $FoM > 4$  are unlikely to be confused with nearby field sources.

To grow the number of known white dwarf debris disks showing a gaseous component, we recommend prioritizing near-infrared spectroscopic follow-up like that in Section 4.3 of the 104 uncontaminated high-confidence variables in our catalog, especially the 84 new discoveries among these, down-weighting the sources we flag as contaminated. Since we are interested in generating a sample of candidate strongly variable debris disks, we have not aimed for completeness in our catalog.

#### 4.2. Characterizing the Variability of Debris Disks with Detected Gaseous Calcium II Emission

In addition to the CVs, the Ca II gas disks appear among the most variable at  $3.4\,\mu\text{m}$ . All six out of six gas disks in our catalog of variables have  $\chi^2 > 6$  (Figure 4, Figure 1a). We publish five out of these six as near-infrared variables for the first time (WD 0145+234 was characterized by Swan et al. 2021).

The six Ca II gas disks in our variable catalog do not include cases like Gaia J0611–6931 (Panel F of Figure 4). Gaia J0611–6931, which might be accreting a disrupted water-rich body (Rogers et al. 2024b), is excluded due to contamination from field crowding, but otherwise does not show obvious evidence for contamination in WISE View, suggesting the apparent brightening towards it could be real and inherent to its debris disk. Likewise, Gaia J2100+2122 and SDSS J2133+2428 show high-amplitude variability ( $\chi^2 > 6$ , see Table 3) and are excluded for having an excess of  $G_{RP}$  flux due to nearby field stars. Both also do not show evidence for contamination in WISE View.

There are seven Ca II gas disk systems that pass our quality filtering and do not exhibit significant variability ( $\chi^2 < 2$ ). Six of these (WD 0842+231, SDSS J0959–0200, WD 1041+092, SDSS J1228+1040, HE 1349–2305, SDSS J1617+1620) were reported to exhibit significant variability in at least one Spitzer IRAC channel ( $3.4\,\mu\text{m}$  or  $4.5\,\mu\text{m}$ ) by Swan et al. (2020), albeit over significantly different light curve baselines ranging from hundreds of days up to about 10 years, and with better sensitivity than provided by WISE. The near-infrared variability towards WD J1930–5028 (Gaia DR3 6646693887514073984), the remaining system, has not been assessed due to the recency of the discovery of calcium triplet emission from its debris disk (Gentile Fusillo

et al. 2021a). Two of these six systems in Swan et al. (2020) have median  $S/N < 10$  in our  $W1$  light curves, whereas all six variable gas disks in our variables catalog have  $S/N > 10$  in  $W1$ . This suggests signal-to-noise in our light curves impacts our determination of variability in some cases, especially when considering the reduced sensitivity in NEOWISE compared to Spitzer+IRAC. When we have robust detections ( $S/N > 10$ ) we find 6/11 gas disks show variability.

Our catalog of variables includes nine white dwarfs with known infrared excesses due to dusty debris disks with no gaseous emission at the calcium triplet yet detected. While all nine appear to show genuine astrophysical variability, it tends to be at a lower level compared to debris disks with gaseous Ca II emission: only six show  $\chi^2 > 3$  (Figure 3). The most extreme of these is GD 56 (Gaia DR3 3251748915515143296), which has  $\chi^2 = 40.0$ . We show the light curve of GD 56 in Panel 9 of Figure 7, where the  $W1$  and  $W2$  fluxes linearly decay until about the year 2020, after which they stabilize to constant values in both channels. The decaying near-infrared flux towards GD 56 was first reported by Farihi et al. (2018). Later analysis by Swan et al. (2021) found this trend to be consistent with the  $t^{-1}$  decay expected from a collisional cascade (Dominik & Decin 2003). We report near-infrared variability towards the non-Ca II debris disks of MCT 0420–7310, KPD 0420+5203, and US 2966 for the first time.

There are 20 non-Ca II disk systems that pass our quality filtering but do not show significant variability ( $\chi^2 < 2$ ). 11 of these 20 systems are included in the survey by Swan et al. (2020), who report significant variability in Spitzer IRAC photometry towards eight. Only four of these eight are reliably bright enough ( $S/N > 10$ ) for us to detect variability, helping explain the why some are not recovered. A total of 8/20 of these non-variable ( $\chi^2 < 2$ ) non-Ca II disks show  $S/N > 10$  in our  $W1$  light curves, yielding a variability rate of 9/17.

We find Ca II (55%) and non-Ca II (53%) disks are variable at roughly the same rates, except disks with observed Ca II gas in emission nearly always show larger flux variations when they are detected to vary. This variability is observed across decade-long baselines with roughly 6 month sampling in our  $W1$  NEOWISE light curves. We do not find commensurate optical variability towards any of these systems in TESS, save the known pulsating white dwarfs EC 11507–519 (0.8% pulsation amplitude in  $V$ -band, Gianninas et al. 2006; Figure 8 Panel 25) and KX Dra (0.5% pulsation amplitude in TESS, Table 2; Figure 8 Panel 35) that also harbor dusty disks. Only KX Dra shows a Gaia EXCESS\_FLUX\_ERROR consistent with optical variability. This underlines that the variability we detect towards these white dwarfs in NEOWISE is intrinsic to their dusty disks.

In Appendix C we show light curves for all 21 published Ca II gas disk systems in Figure 6 and the 47 non-Ca II disks across Figure 7 and Figure 8. We re-

<sup>5</sup> [https://gaia.aip.de/metadata/gaiadr3/allwise\\_neighbourhood/](https://gaia.aip.de/metadata/gaiadr3/allwise_neighbourhood/)

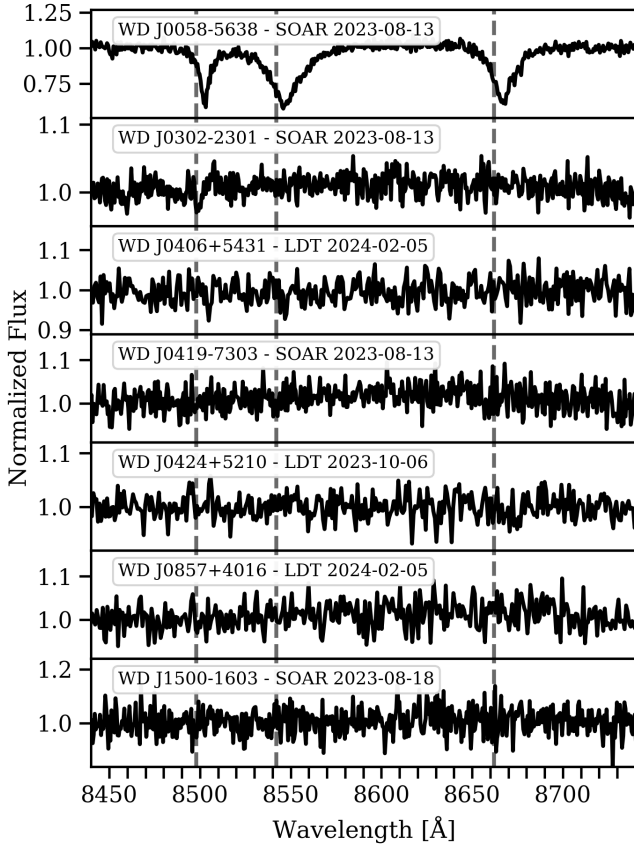


**Figure 5.** Near-infrared spectroscopic follow-up of seven sources from our catalog centered on the calcium triplet region (rest wavelengths marked as dashed grey vertical lines). While we do not detect Ca II gas in emission, we confirm one new remnant planetary system: we observe broad Ca II absorption towards WD J0058–5638 (top panel). Sources are marked with the observatory and UT date of observation.

port our variability parameters for the Ca II disks in Table 3 and for the non-Ca II disks in Table 4.

#### 4.3. Preliminary Searches for Circumstellar Calcium II Emission

We followed up seven objects within our catalog of variables using LDT+DeVeny and SOAR+Goodman as described in Section 2.3, the results of which we show in Figure 5. While we fail to discover new systems showing emission at the calcium triplet, we notably confirm one remnant planetary system, marked by Ca II absorption. The six others show only continua in our wavelength range covering at least 7600 – 8750 Å.

WD J0058–5638 (Gaia DR3 4907742035447425024) shows broad absorption at each line of the triplet likely of photospheric origin ( $S/N = 38.5$ ). We prioritized WD J0058–5638 in our follow-up based on its high degree of variability ( $\chi^2 = 12.8$ ) and red catWISE color (Figure 3). While no higher-resolution spectrum of

WD J0058–5638 is published, Vincent et al. (2024) find its Gaia XP spectra indicate it is spectral type DZ with a probability of 1.0. Photometric fits using He-atmosphere models find it is a 9970 K,  $0.65 M_\odot$  white dwarf (Gentile Fusillo et al. 2021b).

Also included in our follow-up are MCT 0420–7310 (Gaia DR3 4653404070862114176) and KPD 0420+5203 (Gaia DR3 271992414775824640), two systems known to harbor dusty disks. Both show only continua at the calcium triplet region. Our spectra of MCT 0420–7310 ( $S/N=38.9$ ) and KPD 0420+5203 ( $S/N=47.6$ ) are the first published in this region, and suggest their debris disks do not show gaseous calcium in emission at our detection limits.

## 5. DISCUSSION AND CONCLUSIONS

We produce a catalog of 163 unique white dwarfs that appear to show astrophysical variability at  $3.4\mu\text{m}$  in  $W1$  NEOWISE light curves with coverage from 2013–2023 sampled roughly every six months. We generate these light curves using a novel aperture photometry pipeline operating on the unWISE images that corrects for the proper motion of the target. We pass an original input of 3299 white dwarfs, including all 21 published white dwarf Ca II gas disks and most published non-Ca II disks, through quality filtering to eliminate known systematics in effort to include only high-fidelity sources. We further vet the of images of the sources in our catalog of 163 variables, finding 104 are high-confidence variables at  $3.4\mu\text{m}$ , 84 of which are published as variable for the first time.

We find that among sources with uncontaminated photometry and sufficient signal-to-noise (median  $S/N > 10$  in our  $W1$  light curves), 6/11 Ca II gas debris disks and 9/17 of non-Ca II gas disks are variable over baselines of about 9 – 10 years at  $\approx 6$ -month sampling. Due to the substantially dramatic variability shown by the Ca II gas disks, we hypothesize that targeted searches for white dwarfs exhibiting variability at wavelengths  $\lambda \gtrsim 3.4\mu\text{m}$  represents a promising avenue for discovering more white dwarf debris disks showing gaseous emission. We encourage spectroscopic follow-up of the catalog in Table 2 to search for emission at the calcium II triplet indicative of a gaseous debris disk. This is especially motivated by our discovery of one new remnant planetary system, evidenced by calcium triplet absorption towards the white dwarf (Figure 5), though we have not yet discovered a new gas disk in our preliminary follow-up campaign.

Our findings here are in agreement with the work from Swan et al. (2019) and Swan et al. (2020), who found that most debris disks around white dwarfs are variable at  $3.4\mu\text{m}$ , with the Ca II gas disks showing the highest flux variations compared to their non-Ca II counterparts. We also tend to see the degree of variability grow with the light curve baseline, as was observed with Spitzer (Swan et al. 2020). Where there is overlap, all

the Ca II and non-Ca II debris disks both in our catalog of variables are also found to be variable by [Swan et al. \(2020\)](#). We identify at least five new variable Ca II gas disks: LAMOST J0510+2315, SDSS J0347+1624, WD 1622+587, and WD J0529–3401 (Figure 4). We report near-infrared variability towards the non-Ca II debris disks of MCT 0420–7310, KPD 0420+5203, and US 2966 for the first time.

Only 10 of our 104 high-confidence 3.4- $\mu$ m variables show periodic optical variability in TESS. Notwithstanding the differences in sampling and baselines and the determination of variability (empirically based on anomalous scatter in NEOWISE versus significant periodicities in TESS), this suggests that the variability we detect towards these debris disks systems is not intrinsic to the white dwarf photosphere, but rather arises from the dusty components of the disks.

By considering both  $\chi^2_{W1}$  and  $\chi^2_{\text{flat}}$  in our variability ranking, we find at least one more debris disk showing a secular linear trend in flux. The disk around WD J0529–3401 (Panel e of Figure 4) shows a secular decay reminiscent of that towards GD 56 (Panel 9 of Figure 7). Such a decay would be consistent with that expected from a brightening induced by a collisional cascade ([Swan et al. 2024, 2021; Dominik & Decin 2003](#)), albeit over a timescale of at least 10 years. Coupled with the absence of optical variations we find, the heightened 3.4- $\mu$ m variability of the disks showing Ca II emission in our catalog relative to the non-Ca II disks seems to lends further credence to the notion that the photometric variability of these disks is driven by collisions ([Farihi et al. 2018; Swan et al. 2019; Malamud et al. 2021](#)), and that the gaseous disks may be the most the most collisionally active at this moment ([Swan et al. 2020](#)).

Lacking in our analysis is an assessment of the variability seen in our  $W2$ -band (4.6  $\mu$ m) light curves. We only analyze the  $W1$  light curves due to their on-average higher signal-to-noise. Still, the most variable debris disks tend to show significant variability in  $W2$  as well (Figure 4). SDSS J1228+1040, which is not in our catalog of variables and does not appear contaminated, appears to shows more significant flux variations in  $W2$ . Indeed, [Xu et al. \(2018\)](#) found SDSS J1228+1040 shows greater variability at 4.5  $\mu$ m in Spitzer IRAC photometry. We do tabulate calculated  $\chi^2_{W2}$  values in Appendix A. We also do not analyze our PSF-photometry generated light curves since they appear to suffer source detection failures at the lowest signal-to-noise levels, but publish them as well and encourage investigation.

We also plot the WISE cryogenic epochs in our light curves but exclude these fluxes from our variability ranking. Their inclusion would tend to agree with the finding from [Swan et al. \(2020\)](#) that the degree of variability of white dwarf debris disks grows with the light curve baseline (Figure 4). However, there are systematic offsets in flux between the cryogenic and NEOWISE missions

([Meisner et al. 2017a](#)) that make this an unreliable comparison.

Unlike their hosts’ photospheres, the future for the study of remnant planetary systems around white dwarfs is bright in the infrared. The Near-Earth Object Surveyor, the successor to WISE and NEOWISE, is planned to launch as early as 2028 and survey the sky at 4.6 and 8  $\mu$ m ([Mainzer et al. 2023](#)). SPHEREx will compliment NEO Surveyor with spectra spanning 0.75 – 5  $\mu$ m covering the entire sky ([Doré et al. 2018](#)). Large, deep spectroscopic surveys like DESI and SDSS-V should discover more gaseous debris disks from their emission at the near-infrared calcium triplet, with target selection propelled by the discovery of hundreds of thousands high-probability white dwarf candidates with Gaia ([Gentile Fusillo et al. 2021b](#)). JWST is already characterizing gaseous debris disks ([Swan et al. 2024](#)), with surely more on the way. We expect that near-infrared variability will aid in efficiently identifying the most compelling targets for the next generation of flagship observatories like JWST.

## 6. ACKNOWLEDGMENTS

We thank the anonymous referee for their constructive comments and suggestions that improved this paper.

This material is based upon work supported by the National Aeronautics and Space Administration under Grant No. 80NSSC23K1068 issued through the Science Mission Directorate. Support for this work was in part provided by NASA TESS Cycle 4 grant 80NSSC22K0737 and Cycle 6 grant 80NSSC24K0878. JAG is supported by the National Science Foundation Graduate Research Fellowship Program under Grant No. 2234657. JAG recognizes Siyi Xu (许偲艺, Gemini Observatory) for numerous fruitful discussions that improved this study and the interpretation of these results. K. D. was supported by NASA through the NASA Hubble Fellowship grant #HST-HF2-51477.001 awarded by the Space Telescope Science Institute, which is operated by the Association of Universities for Research in Astronomy, Inc., for NASA, under contract NAS5-26555. This research was improved by discussions at the KITP Program “White Dwarfs as Probes of the Evolution of Planets, Stars, the Milky Way and the Expanding Universe” supported by National Science Foundation under grant No. NSF PHY-1748958.

This publication makes use of data products from the Wide-field Infrared Survey Explorer, which is a joint project of the University of California, Los Angeles, and the Jet Propulsion Laboratory/California Institute of Technology, funded by the National Aeronautics and Space Administration. This publication also makes use of data products from NEOWISE, which is a project of the Jet Propulsion Laboratory/California Institute of Technology, funded by the Planetary Science Division of the National Aeronautics and Space Administration.

These results make use of the Lowell Discovery Telescope at Lowell Observatory. Lowell is a private, non-profit institution dedicated to astrophysical research and public appreciation of astronomy and operates the LDT in partnership with Boston University, the University of Maryland, the University of Toledo, Northern Arizona University, and Yale. We particularly thank LDT telescope operators Ishara Nisley and Cecilia Siqueiros.

Our work is based on observations obtained at the Southern Astrophysical Research (SOAR) telescope, which is a joint project of the Ministério da Ciência, Tecnologia e Inovações (MCTI/LNA) do Brasil, the US National Science Foundation’s NOIRLab, the University of North Carolina at Chapel Hill (UNC), and Michigan State University (MSU). We particularly thank Sean Points and Felipe Navarete for observing on our behalf and Jay Elias for facilitating our observing plan.

This work has made use of data from the European Space Agency (ESA) mission *Gaia* (<https://www.cosmos.esa.int/gaia>), processed by the *Gaia* Data Processing and Analysis Consortium (DPAC, <https://www.cosmos.esa.int/web/gaia/dpac/consortium>).

[cosmos.esa.int/web/gaia/dpac/consortium](https://www.cosmos.esa.int/web/gaia/dpac/consortium)). Funding for the DPAC has been provided by national institutions, in particular the institutions participating in the *Gaia* Multilateral Agreement.

This paper includes data collected by the TESS mission. Funding for the TESS mission is provided by the NASA’s Science Mission Directorate.

*Facilities:* WISE, NEOWISE, Gaia, LDT, SOAR, TESS, ASAS-SN

*Software:* Astropy (Astropy Collaboration et al. 2013, 2018), lmfit (Newville et al. 2014), Matplotlib (Hunter 2007), NumPy (Harris et al. 2020) pandas (pandas development team 2020), PypeIt (Prochaska et al. 2020), SciPy (Virtanen et al. 2020), seaborn (Waskom 2021), TOPCAT (Taylor 2005), SIMBAD and VizieR (curated by CDS, Strasbourg, France), and the NASA Astrophysics Data System (ADS).

## APPENDIX

### A. VARIABILITY RANK TABLES

Here we show various tables summarizing our variability ranking and validation for the various inputs in our sample. In Table 2 we show these parameters for our catalog of variables, which includes all 104 high-confidence variables and the 59 likely contaminated sources. In Table 3 we show these parameters for the 21 previously published white dwarf debris disks that show gaseous calcium in emission. In Table 4 we show these parameters for the 47 disks in our study that do not show gaseous emission.

**Table 2.** Variability Parameters for our Catalog of 163 Variable White Dwarfs

Gaia DR3 Source ID	R.A. (J2000)	Decl. (J2000)	Sample	Flag	$\chi^2_{W1}$	$\chi^2_{\text{alt}}$	$\chi^2_{W2}$	S/N	G <sub>RP</sub>	E <sub>Excess</sub>	G <sub>RP</sub>	W1 (mag)	W1 – W2 (mag)	Spectral Type	T <sub>eff</sub> (K)	M <sub>WD</sub> ( $M_\odot$ )	E <sub>FF</sub>	F <sub>oM</sub>	TESS (hr, %)	
231282126330222720	0.66720	-34.22766	GC	*	1.3	1.9	2.2	5.1	0.000	14.5	20.2	-0.3	DC [1]	6460	0.73	1.8	9.3			
5377631217585252600	1.28048	73.21927	GC	*	2.5	3.1	2.6	1.0	0.231	14.3	17.8	-0.8	DBZA [2]	14.160	0.66	1.4	7.6			
497879341987799040	7.69668	-47.21010	GC	2	47.1	68.1	46.5	4.0	0.000	15.2	19.0	-0.8	DA [3]	13600	0.31	0.3	9.0			
38139632999329408	9.98592	42.49150	GC	*	2.1	2.8	2.3	0.0	0.295	16.4	19.5	-0.8	DA [4]	9990	0.55	0.0	7.6			
414603086333416224	12.18956	50.12801	GC	*	2.4	3.7	2.3	0.9	18.5	0.361	16.1	18.7	-0.8	DA [5]	10130	0.76	0.0			
45077423047425024	14.56330	-56.6316	GC	*	12.0	18.9	12.8	4.9	14.3	0.560	16.9	19.1	-0.2	DZ [5]	10250	0.74	0.7	8.5		
5026963366179.4939520	17.15014	-32.62872	IR, GC	2.2	2.6	2.5	0.9	28.9	1.110	15.5	18.1	-0.7	DAZ [3]	16050	0.63	0.0				
49138920392437776	18.0809	-56.24098	IR, GC	2.6	4.1	2.7	1.1	20.4	0.000	15.9	18.8	-0.3	DBAZ [6]	18790	0.59	0.0	8.7			
3218563324222336	18.88398	37.62655	CV	137.5	203.3	156.3	12.8	23.5	0.000	17.2	18.3	-0.5	CV [7]				7.7			
40995690043661312	19.72331	52.45381	GC	*	1.5	2.5	2.1	0.5	15.5	0.475	15.6	18.9	-0.7	DA [3]	10760	0.60	0.7	5.1		
4704847730628098048	21.6348	-65.94308	GC	*	2.5	4.0	2.4	0.9	19.7	0.572	15.6	19.0	-0.9	DA [8]	13400	0.76	1.2	6.7		
248073179699826176	22.59595	-4.79939	GC	1	1.2	1.9	3.4	0.9	12.1	0.355	15.0	19.0	-0.7	DA [3]	16280	0.57	0.0	9.0		
4686195252815125888	22.74033	-73.83004	GC	1	1.9	2.4	14.6	1.0	28.7	0.566	16.4	18.7	-0.6	DA [9]	7820	0.52	0.0			
49124275947846613760	23.99450	-54.73145	GC	*	2.1	2.1	2.3	1.1	27.5	0.360	15.4	18.5	-0.7	DA [5]	10310	0.61	1.3	8.0		
57248774053132288	25.36576	83.58301	GC	*	2.1	2.4	2.7	1.6	98.0	0.013	13.3	16.8	-0.7	DA [3]	19000	0.65	0.3	10.4		
5135466183642594304	26.84096	-21.94761	GC	[a]	1.4	2.1	2.4	0.9	65.6	0.000	15.2	16.9	-0.5	DA [3]	11080	0.60	7.8	8.9	0.12, 0.5	
29105743312534464	26.97841	23.66211	Ca, II, GC	422.6	690.7	482.4	254.9	54.3	0.021	14.1	16.9	-0.4	DA [10]	12980	0.66	0.8				
2574771753493428648	28.77645	12.146959	GC	*	2.2	3.4	2.1	6.6	0.000	17.0	19.8	-0.4	DA [5]	7810	0.61	0.0	6.9			
4970215730470383616	33.45361	-33.75834	GC	1	1.7	1.8	10.8	0.9	25.4	0.555	15.1	18.3	-0.7	DAZ [1]	4640	0.37	2.4	1.4		
5063539946887524864	37.11129	-32.70939	GC	*	2.1	2.4	2.1	1.1	34.4	0.011	14.1	17.9	-0.7	DA [3]	22280	0.63	0.3	8.0		
4945883969667016960	39.19143	-44.87680	GC	*	2.1	2.6	2.0	6.7	0.000	16.6	20.2	-0.8	DA [5]	15690	0.77	1.9	6.2			
5484232788111480960	40.38260	74.71518	GC	1	1.3	2.1	3.7	0.9	15.5	0.505	15.8	19.1	-0.7	DA [3]	9130	0.60	0.0	9.3		
5052391205216637440	43.82287	-32.11233	GC	*	2.2	2.5	2.2	6.6	0.000	17.0	19.9	-0.7	DA [5]	6770	0.83	1.5	8.2			
45.65272	* 2.5	3.5	2.5	0.0	8.4	0.105	15.9	19.6	-0.7	DA [3]	22880	0.86	1.2	7.9						
4733604373137759616	48.32741	-56.12639	GC	[1, b]	1.3	1.7	11.9	1.0	52.4	0.636	14.6	17.9	-0.8	DA [11]	10980	0.60	6.1	0.22, 0.2		
484744374331819136	49.20349	-44.62911	GC	*	1.8	2.6	2.5	0.8	22.4	0.200	17.0	18.8	-0.8	DA [5]	5590	0.64	0.8			
5098597840775610112	50.37700	-22.45211	GC	*	2.7	2.8	2.7	0.0	7.8	0.038	16.7	19.7	-0.6	DA [5]	5210	0.38	13.0	4.2		
5053839127592396032	52.21176	-32.64194	GC	1	1.2	1.3	5.0	0.9	13.0	1.399	16.6	19.2	-0.7	DC [1]	4640	0.45	1.1	8.5		
63126196662629416	55.84366	19.97044	GC	*	2.0	2.6	2.0	0.6	27.8	0.487	15.3	18.0	-0.6	DA [12]	7110	0.87	0.0	8.9		
430295287784160	56.90288	-16.40270	Ca, II	*	12.3	17.7	12.1	0.5	11.2	0.440	16.7	19.2	-0.4	DAZ [13]	17110	0.52	0.0	6.9		
57008653335107200	57.49233	82.90492	GC	*	2.2	3.1	2.1	0.4	12.8	0.153	16.2	19.6	-0.8	DA [5]	13430	0.61	1.2	6.0		
5094843764483219712	58.42161	-19.93029	GC	*	2.2	3.0	2.1	0.5	8.8	0.000	16.5	19.6	-1.0	DA [5]	10250	0.59	2.6	7.1		
276192136857805656	61.52921	54.52561	GC	*	3.6	4.5	3.4	0.3	8.9	0.945	15.5	19.5	-0.8	DA [3]	17010	0.63	0.9			
325174891515143296	62.75904	-3.97294	IR	4.9	6.8	40.0	3.3	56.2	0.268	15.7	17.1	0.2	DA [3]	14900	0.61	0.1	10.7			
229143725086190336	64.52301	42.18394	GC	1	1.3	2.0	3.3	1.9	23.1	0.989	16.4	18.3	-0.7	DA [14]	5650	0.49	0.2			
4867104257483687040	71.11395	-35.29586	GC	*	1.5	2.4	3.9	3.5	1.3	59.6	0.150	15.7	17.7	-0.1	DA [3]	17790	0.58	0.0	9.6	
23299507267507296	65.37243	46.13271	GC	1	1.2	2.2	1.1	41.0	0.996	14.9	17.6	-0.8	DA [14]	7810	0.59	0.0	7.0			
271929411758241640	66.06347	52.16962	IR, GC	*	3.1	4.9	17.4	2.2	40.1	0.876	15.2	17.6	-0.3	DA [3]	22170	0.66	0.9			
3186021141200137472	69.44754	-8.81962	GC	2	6.8	7.4	23.1	1.3	14.2	0.073	13.2	19.1	-0.8	DQ [15]	6720	0.66	1.8			
34157882558117248	77.50894	23.26151	Ca, II, GC	*	41.9	65.9	49.5	16.0	41.8	0.796	15.2	17.4	-0.1	DAZ [19]	21250	0.73	0.0	9.0		
4823042355496728832	82.30968	-54.01892	Ca, II	*	2.0	2.2	6.4	0.8	28.5	0.230	17.6	18.4	0.1	DAZ [20]	17190	0.46	0.0			
4805197659735412224	86.36308	-39.59992	GC	*	1.4	1.5	2.2	1.0	31.4	0.085	16.3	18.4	-0.7	DA [5]	5220	0.27	0.0	8.9		

**Table 2** continued

Table 2 (continued)

Gaia DR3 Source ID	R.A. (J2000)	Decl. (J2000)	Sample	Flag	$\chi^2_{W_1}$	$\chi^2_{\text{alt}}$	$\chi^2_{\text{flat}}$	$\chi^2_{W_2}$	S/N	G <sub>RP</sub>	E <sub>Excess</sub>	G <sub>RP</sub>	W <sub>1</sub>	W <sub>1</sub> – W <sub>2</sub>	Spectral (mag)	$T_{\text{eff}}$ (K)	$M_{\text{WD}}$ ( $M_{\odot}$ )	EFF	FoM	TESS (hr, %)
3429193393407592576	87.69361	26.20574	GC	*	2.5	3.3	2.4	0.8	9.7	0.822	15.6	19.2	-0.8	DA [21]	21210	0.57	0.0			
32186977678376320	87.83117	-0.17253	GC	*	2.2	2.6	1.2	59.0	0.015	14.0	17.0	-0.7	DQ [1]	6180	0.72	4.5	9.5			
3022568258012024	88.03243	-5.41682	CV	2	1216.6	1640.3	1152.6	526.6	81.3	0.113	13.5	-0.5	CV [22]					10.1		
4650712810002383104	89.51038	-72.48012	GC	1	1.1	1.5	2.6	1.2	14.8	1.284	16.7	-0.8	DC [1]	6850	0.83	0.0	7.1			
1114054838014073984	91.81668	73.51325	GC	1	0.2	0.2	6.0	5.5	0.8	10.1	0.049	16.6	-0.5	DA [14]	6520	0.92	1.3	6.6		
943770757500160384	101.90802	37.51585	GC	2	2.3	2.9	0.0	2.3	0.0	11.3	0.063	12.3	-0.7	DA [3]	213390	0.71	0.2	10.5		
950478049312082688	104.43818	40.12384	GC	3	1.7	2.4	15.8	1.2	14.0	0.514	14.3	-0.7	DA [14]	6580	0.46	0.6	7.8			
5336077246353138240	113.40764	-42.89924	GC	*	2.1	2.1	2.0	2.0	24.4	0.891	15.3	-0.7	DA [10]	15020	0.70	0.3				
5295191102987133824	115.47008	-57.14576	GC	*	2.1	3.1	2.1	0.7	8.0	0.690	16.4	-0.9	DA [23]	19640	0.47	0.0	0.06, 0.7			
3150770626615542784	117.92301	11.34175	GC	*	367.0	520.4	346.0	245.6	98.9	0.626	15.1	-0.4	CV [24]	11810	0.56	0.8	6.1			
5210507852302442368	121.86563	-76.53352	CV	499.9	956.4	489.1	288.5	92.0	0.028	14.3	15.9	-0.4	CV [25]	111.8	2.2					
10910510962545384	123.11779	62.60623	CV	*	1.9	2.5	2.2	2.2	5.9	0.084	16.2	-0.9	DA [10]	7640	0.62	0.0	5.6			
908364559240386944	125.00536	38.57553	GC	*	1.4	2.2	2.1	1.2	17.1	0.000	15.6	-0.5	DA [3]	11570	0.61	3.4	0.14, 0.9			
911639111029648512	130.03196	40.25104	GC	[c]	51.2	76.7	49.9	6.9	20.6	0.089	11.7	-0.8	DA [3]	9080	0.47	0.9	7.3			
56393770626615542784	130.38422	-32.94248	GC	*	2.5	2.9	2.5	1.1	41.3	0.218	15.1	-0.2	DZ [5]	5520	0.75	4.4	10.3			
573473743856734432	130.70190	-13.78700	GC	*	2.0	2.3	2.8	1.8	35.8	0.386	15.2	-0.8	DA [5]	9190	0.42	0.0				
552244655095424288	131.23160	-44.14232	GC	1	2.0	2.3	2.9	1.4	17.6	0.364	15.4	-0.8	DA [26]	9610	0.58	0.4	2.5			
910341618586847232	131.35268	38.03232	GC	*	2.6	3.0	2.5	0.6	19.4	0.044	15.7	-0.7	DA [3]	8000	0.58	0.0	8.0			
1037258898615762048	131.51030	57.05795	Ca II	*	25.2	37.1	26.1	9.0	95.4	0.900	16.9	0.0	DA [3]	15410	0.57	0.1	8.0			
5220278609486918286	131.94610	-73.21382	GC	1	0.9	1.9	2.2	0.5	26.4	0.443	15.4	-0.8	DA [3]	17030	0.54	0.5				
562244655095424288	131.37693	40.37029	GC	*	2.0	2.3	2.3	1.1	15.2	0.248	15.0	-1.0	DA [3]	22600	0.61	0.4	9.1			
56292614773212856	134.79068	-36.79189	GC	1	3.0	4.0	2.9	1.4	17.6	0.364	15.4	-0.8	DA [5]	9190	0.42	0.0				
71288809065563624	134.81103	32.95338	GC	2	2.8	3.4	2.8	0.9	17.0	0.068	15.0	-0.7	DQ [3]	10370	1.05	2.4	8.9			
711744456827031680	135.67776	31.34542	GC	3	2.7	4.0	2.9	0.9	15.3	0.000	15.1	-0.8	DA [3]	9840	0.74	0.1				
1123702356048742016	136.38352	73.24860	GC	2	2.2	2.5	2.1	0.2	9.4	1.059	16.1	-0.5	DC [14]	5130	0.57	0.7	9.7			
56353449564642200576	136.66879	-30.20627	GC	3	3.2	3.6	3.9	0.6	19.3	0.335	15.7	-0.6	DA [5]	9580	0.59	0.0	1.8			
69212461773212856	136.89278	27.65095	GC	*	2.1	2.1	1.6	28.1	0.0	0.953	16.2	-0.8	DA [21]	14660	0.81	0.0				
59104086489874312	139.01121	10.18630	GC	2	2.3	2.7	2.2	1.2	15.9	0.258	15.6	-0.9	DQZ [27]	9460	0.78	0.0	8.9			
334355753438777152	140.73361	1.02582	GC	1	1.1	1.4	4.3	1.6	34.6	0.269	16.1	-0.7	DAZ [28]	6600	0.57	0.0				
5669427512497660800	153.00767	-18.72591	GC	*	6.7	7.6	6.4	0.3	9.1	0.000	15.0	-0.5	DZ [2]	6520	0.75	0.7	9.8			
38300623164560911872	154.02864	-1.32143	GC	2	1.5	1.7	2.6	1.0	8.1	0.677	15.0	-0.1	DA [3]	7760	0.29	0.4	10.2			
5446683430923603840	155.40966	-34.80381	GC	*	2.1	3.2	2.0	0.0	6.3	0.559	16.3	-0.8	DA [26]	14210	0.57	1.2	6.1			
86104086489874312	157.22873	11.09741	GC	1	1.5	1.8	2.3	0.9	19.7	1.252	15.7	-0.5	DA [3]	14710	0.62	0.2				
1076941716370493696	159.24298	71.18298	GC	1	3.7	5.9	3.9	0.0	10.8	1.202	15.9	-0.5	DC [29]	4690	0.68	0.2	2.2			
539448730327131904	160.94445	-39.11038	GC	*	2.0	2.9	1.9	0.0	10.8	0.717	15.4	-0.7	DA [5]	25710	0.63	2.1				
3355523756458520000	162.83398	-1.17569	GC	*	2.2	3.0	2.0	0.0	6.9	0.601	16.9	-0.7	DA [5]	9150	0.60	0.0	4.6			
37634454092857824	164.39036	-7.52310	GC	3	8.1	13.2	105.4	1.2	13.4	0.196	14.0	-0.6	DC [30]	7520	0.87	0.5				
86104086489874312	166.92737	59.97490	GC	*	2.6	2.9	2.5	1.1	52.6	0.003	14.0	-0.7	DA [3]	18310	0.69	0.0	10.1			
4019780359821201536	168.90400	55.5475	IR	*	2.5	2.9	2.4	0.4	10.4	0.000	16.7	-0.8	DA [3]	5050	0.39	0.0	9.0			
3817262208497857024	169.16826	6.45074	GC	*	2.5	2.7	2.6	0.2	8.9	0.000	16.2	-0.7	DA [3]	6260	0.54	0.0	8.6			
379004046528127616	169.56276	-3.23488	GC	1	4.5	7.2	13.1	0.0	6.9	0.000	15.2	-0.7	DQ [30]	9900	0.70	0.0				
35400018805367474816	175.48576	-23.34921	GC	*	2.2	2.4	2.1	7.1	0.433	16.5	19.8	-0.7	DA [3]	13410	0.60	0.5				
1074721664954807040	175.91038	71.68904	CV	411.4	623.4	405.7	352.3	135.4	0.019	14.4	-0.4	CV [31]					11.2	3.97, 3.0		
34662368113347520	176.99441	28.53223	IR, GC	[d]	4.6	6.6	4.3	3.2	40.5	0.046	16.0	-0.7	DA [3]	11770	0.62	0.1	9.4			
112925142873666848	178.67584	79.24235	GC	2	2.8	3.0	2.8	0.2	13.1	0.000	15.8	-0.8	DA [3]	10470	0.57	0.4	8.4			
34662368113347520	181.69334	-32.57586	GC	2	2.2	3.1	0.5	13.5	0.054	15.8	19.1	-0.6	DA [3]	19970	0.61	0.0				
3576269871237617024	184.79672	-12.89442	GC	1	3.2	5.0	8.2	1.9	25.3	0.257	16.4	18.2	-0.4	DA [5]	8310	0.58	0.0			
154372370905857792	188.73446	47.62593	GC	*	2.7	3.0	2.7	1.4	33.4	0.000	14.6	-0.8	DA [3]	15230	0.59	0.4	9.7			

Table 2 continued

Table 2 (continued)

Gaia DR3 Source ID	R.A. (J2000)	Decl. (J2000)	Sample	Flag	$\chi^2_{W1}$	$\chi^2_{\text{alt}}$	$\chi^2_{\text{flat}}$	$\chi^2_{W2}$	S/N	G <sub>RP</sub>	E <sub>Excess</sub>	G <sub>RP</sub>	W1	W1 – W2	Spectral	$T_{\text{eff}}$	$M_{\text{WD}}$	E <sub>FF</sub>	F <sub>oM</sub>	TESS
									(mag)	(mag)	(mag)	(mag)		(mag)	Type	(K)	( $M_{\odot}$ )	(hr, %)		
612733286605955072	189.70606	-49.80006	GC	[e]	2.2	2.6	0.8	27.6	0.764	13.8	18.1	-0.6	DA [3]	11350	1.04	0.9	9.0	0.16, 0.1		
1540371883066128768	191.39846	42.64019	GC	2	2.0	3.0	1.9	8.2	0.058	17.0	19.9	-0.7	DA [27]	9540	0.80	0.0	0.0	0.0		
3393156211047680	196.42659	18.01771	GC	5.1	5.3	1.7	14.6	0.100	15.9	18.9	-0.0	CV [32]	11530	0.53	10.1	8.7	0.78, 1.1			
374364635656365352	198.42576	13.68691	GC	*	2.3	3.6	2.3	5.7	0.119	16.9	20.1	-0.4	DC [33]	9710	0.91	0.0	6.6	0.0		
3506567228052533120	199.08138	-20.12557	GC	1	1.1	1.3	4.5	0.3	9.5	0.549	16.4	19.2	-0.9	DZ [34]	5230	0.83	19.6			
33303578797247600	202.55677	-8.57485	GC	3	108.0	163.9	108.8	14.8	45.4	0.044	12.5	17.1	-0.5	DA [3]	14560	0.59	0.3	4.2		
1470081444731625728	202.79520	34.14484	GC	*	3.2	4.8	3.1	0.6	18.1	0.041	15.3	18.8	-0.8	DA [3]	16720	0.55	0.6	8.5		
371491427170553360	205.34082	5.01273	GC	2	1.7	1.8	2.3	1.6	17.0	0.050	15.5	18.7	-0.4	DC [28]	4020	0.44	0.0	10.0		
144416124019904768	207.63476	24.57086	GC	*	2.4	3.9	2.3	0.0	8.3	0.000	16.2	19.6	-0.9	DA [23]	13140	0.67	0.4	7.6		
364471766981737856	210.64444	-4.91747	GC	3	1.2	1.2	2.6	0.7	15.2	0.170	16.4	18.7	-0.9	DA [34]	555	0.55	0.0			
621773938701063808	221.84281	-30.58990	GC	*	2.2	5.1	1.9	4.0	0.365	19.4	20.4	-0.6	DA [35]	7100	0.63	0.0	7.1			
6306842338087328512	225.01548	-16.06410	GC	*	1.8	6.3	2.1	7.8	0.103	16.9	19.6	-0.7	DA [5]	7150	0.60	0.0	5.6			
1164184283975493120	233.32823	7.29944	GC	*	1.8	2.6	2.1	6.4	0.000	16.6	20.0	-1.3	DA [23]	10260	0.54	0.7	5.6			
1641326679142898048	235.43704	64.89805	IR, GC	[f]	1.9	2.5	3.2	1.6	65.7	0.188	15.6	17.8	0.2	DAV [36]	11600	0.63	10.2	10.5	0.19, 0.5	
1598737421796352	237.14875	57.14068	GC	2	2.1	2.2	0.9	16.7	0.000	16.9	19.4	-0.7	DB [37]	5910	0.75	0.9	8.2			
1596309737421796352	237.84308	71.75239	CV		39.8	54.1	42.1	6.8	45.2	0.000	16.5	18.2	-0.5	CV [38]			6.2	1.63, 0.7		
440673320701806944	241.47717	-0.46974	GC	*	2.3	3.4	2.2	8.2	0.527	16.5	19.6	-0.7	DA [3]	9350	0.59	0.1	7.7			
1429618420396285952	243.31921	55.35721	GC	*	2.1	2.9	2.4	1.3	29.0	0.041	16.0	18.7	-0.3	DA [3]	11980	0.66	0.6	8.9		
1623866184737702912	245.74852	58.67725	Ca II	*	9.8	14.8	9.2	2.9	20.9	0.152	17.0	19.2	-0.2	DB [3]	18790	0.48	1.5			
16531044367185115264	247.16083	70.88936	GC	*	3.2	3.4	2.5	4.9	0.000	16.9	20.9	-0.5	DA [14]	4900	0.57	0.3	8.4			
170571041903191872	251.78941	77.21274	GC	*	2.4	3.9	2.4	9.8	0.242	15.1	18.8	-0.8	DB [3]	15260	0.61	0.0	9.2			
4379328051494006784	253.15663	-1.23234	GC	*	2.0	2.6	2.1	0.2	7.8	0.468	16.6	19.1	-1.0	DA [23]	12740	0.57	1.1	5.5		
45650483124887877888	254.29109	21.44685	GC	2	4.3	5.4	4.4	0.7	7.8	0.199	13.9	19.8	-0.7	DA [3]	9200	0.60	0.0	10.1		
163865633220634368	258.27492	69.52375	GC	2	67.1	68.2	59.7	0.6	62.6	0.000	13.4	17.7	-0.7	DC [1]	15730	0.61	0.0	10.4		
134827510276198912	261.87223	42.08119	GC	2	2.7	3.8	2.5	1.1	10.7	0.316	16.5	19.3	-0.8	DA [5]	9580	0.65	0.0			
591319751041903191872	262.59637	-57.92381	GC	*	2.5	4.0	2.4	7.5	0.911	15.4	19.6	-1.0	DBA [39]	14060	0.61	0.4	6.5			
170663109358103872	263.40091	79.82129	GC	1	1.1	1.8	2.4	1.3	28.1	0.346	16.5	18.9	-0.7	DC [14]	5760	0.84	1.0			
4595779373528796528	265.13949	23.34029	GC	*	3.1	3.5	3.2	6.4	0.000	16.7	20.2	-0.5	DC [5]	7170	0.75	0.0	7.7			
5920900901901635968	266.90216	-54.60866	GC	1	1.3	2.0	4.7	1.5	28.6	1.139	15.2	18.0	-0.6	DC [1]	4350	0.47	0.8			
141720020676904704	269.49775	54.68952	GC	2	2.7	3.8	2.5	1.1	10.7	0.316	16.8	19.8	-0.7	DA [14]	7670	0.56	0.0			
4470733174161338704	271.84740	3.95050	GC	2	2.6	2.7	0.9	33.1	0.582	14.5	17.8	-0.8	DA [3]	10220	0.64	0.1				
44707414466452138496	274.27702	13.73761	GC	5.6	5.8	0.1	9.7	0.818	15.0	19.5	-0.5	DA [26]	4570	0.48	0.3					
2158251858508357504	275.33333	61.01872	GC	1	1.2	1.3	4.5	1.7	6.6	0.157	14.7	20.3	-0.6	DA [3]	4820	0.46	0.0	3.5		
2256410856215182464	278.82519	64.35491	GC	*	2.2	2.3	2.0	0.6	25.9	0.045	16.7	18.7	-0.7	DC [1]	4900	0.58	1.1	9.5		
215646995191226112	279.53127	60.36160	GC	*	2.9	3.2	2.8	0.6	40.7	0.024	15.6	18.4	-0.7	DA [5]	8990	0.52	0.0			
2127566548919332608	281.61211	46.33753	GC	2	3.0	2.2	0.8	29.1	0.826	15.6	18.6	-0.9	DA [40]	8140	0.72	0.4	7.7	4.66, 2.4		
67404393754556117784	286.22801	-36.05303	GC	*	1.9	2.7	2.0	1.1	42.0	0.126	14.1	17.5	-0.7	DA [26]	13080	0.67	0.8			
1831553382794173824	286.25519	73.74796	GC	*	1.3	1.3	2.2	1.5	21.7	1.387	16.5	19.0	-0.9	DA [5]	8330	0.56	0.0			
2263690864438162944	287.69110	71.92769	GC	*	2.0	2.7	2.0	0.9	14.2	1.258	16.7	19.5	-0.8	DA [3]	11870	0.72	0.0			
4235280071072332672	289.12178	-1.04241	GC	1	63.3	96.7	592.3	7.8	35.8	0.519	13.3	17.6	-0.8	DAH [1]	7790	0.70	12.0			
642746856182061312	302.09959	-66.07714	GC	*	2.2	2.8	2.4	1.4	14.2	0.208	16.1	18.9	-0.2	DA [17]	21380	0.72	1.1			
4223980836743666176	304.46180	-1.44747	GC	*	2.2	3.5	2.1	7.2	1.211	15.7	19.7	-0.7	DA [5]	16260	0.57	0.4	7.8			
1831553382794173824	308.59100	25.06382	GC	1	1.3	1.7	16.7	1.2	0.072	11.7	18.8	-0.7	DA [37]	20140	0.59	0.3	10.3			
647110260640813360	309.57045	-53.07371	GC	*	2.0	2.6	1.2	28.7	0.103	14.4	18.2	-0.7	DB [3]	15720	0.40	0.1	6.7			
668332127247191848	309.67782	-36.82044	GC	*	1.9	2.4	2.3	0.9	28.4	0.215	14.8	18.0	-0.8	DA [3]	9490	0.62	0.0	9.2		
668177394773560192	310.95503	-39.05501	GC	1,[g]	3.1	3.7	2.9	1.5	34.1	1.187	13.7	17.6	-0.1	DA [3]	11220	0.63	6.7	0.3	0.17, 0.3	
6794613322139870080	312.37830	-30.08413	GC	*	2.9	4.5	2.9	0.2	13.3	0.971	15.4	18.9	-0.8	DBA [39]	12030	0.70	0.0	6.5		
2221406155496413952	317.46853	65.12276	GC	*	2.1	3.6	2.3	1.1	21.8	0.144	15.5	19.0	-0.8	DAH [26]	21400	0.88	0.0	0.4		

Table 2 continued

Table 2 (continued)

Gaia DR3 Source ID	R.A. (J2000)	Decl. (J2000)	Sample	Flag	$\chi^2_{W1}$	$\chi^2_{\text{alt}}$	$\chi^2_{\text{flat}}$	$\chi^2_{W2}$	S/N	G <sub>RP</sub>	E <sub>Excess</sub>	G <sub>RP</sub>	W1	W1 – W2	Spectral	$T_{\text{eff}}$	$M_{\text{WD}}$	E <sub>FF</sub>	F <sub>oM</sub>	TESS
										(mag)	(mag)				(mag)		( $M_{\odot}$ )			(hr, %)
2690763205257368832	317.94327	1.34841	GC	2	2.2	3.0	2.6	8.1	0.813	15.4	19.4	-0.7	DA [14]	15730	0.58	0.3	8.2			
6896767366186700416	318.03555	-8.82688	CV	35.1	41.7	34.5	8.4	51.2	0.000	16.4	17.3	-0.3	CV [41]			34.3	10.3	1.54	7.1	
6583253508476544	320.52351	-88.64296	GC	2	182.1	272.5	180.1	16.7	24.0	0.059	15.7	18.7	-0.7	DC [1]	5100	0.47	0.0	7.9		
6583253508476544	320.52351	-88.64296	GC	2	2.0	2.4	2.0	0.9	13.7	0.434	15.8	19.4	-0.7	DB [5]	11250	0.74	0.0			
2220815323910913920	320.63282	66.01214	GC	*	2.7	3.2	2.6	6.8	0.511	16.7	19.9	-0.9	DA [23]	9840	0.63	0.0	5.2			
1785059485263249408	320.77531	1.928408	GC	*	2.3	3.0	2.1	0.0	10.2	0.057	15.4	19.2	-0.9	DA [3]	15020	0.69	0.0	8.0		
6828110179364684672	321.60953	-22.73151	GC	*	2.1	3.1	2.4	0.0	7.1	0.000	16.9	19.7	-0.5	DA [5]	7460	0.53	0.0	7.0		
6830482410058056192	325.89003	-19.20734	GC	*	2.1	3.1	2.4	0.0	7.1	0.000	16.9	19.7	-0.5	DA [5]						
2673699059671833984	328.42542	-2.24063	GC	*	2.1	3.4	2.1	0.3	9.9	0.081	17.0	19.4	-0.9	DA [5]	6620	0.56	0.0	2.3		
26736637246334720	329.69637	-2.67345	GC	2	2.2	2.9	2.1	1.3	19.1	0.000	16.5	18.6	-0.7	DC [1]	4730	0.48	0.0	9.2		
6613289285448236288	331.15850	-31.45382	GC	1	1.8	2.4	5.4	1.6	11.5	0.068	16.2	19.1	-0.2	DA [11]	4810	0.53	0.1	0.2		
2595728287804350720	336.07265	-16.26310	IIR, GC		1.6	2.3	3.4	0.7	19.5	0.663	15.9	18.5	-0.4	DAZ [6]	9900	0.67	0.0	8.2		
2737918849495239936	337.11568	17.90141	GC	*	2.4	3.7	2.4	2.4	8.5	0.280	16.3	19.6	-1.0	DA [23]	14650	0.59	0.7	7.0		
2623101763649861632	337.14432	-6.20543	GC	*	2.2	3.3	2.2	1.4	12.9	0.000	16.3	19.0	-0.9	DA [5]	6940	0.54	0.6	8.1		
284245015383734928	346.57374	24.53547	GC	[h]	2.2	3.4	2.1	1.2	20.3	0.000	15.3	18.5	-0.7	DA [3]	11430	0.60	10.0	8.8	0.22	, 1.7
2407167579853954688	348.87669	-14.66824	GC	2	2.9	4.2	2.7	0.5	20.5	0.079	15.3	18.4	-0.8	DA [35]	8850	0.84	0.0	7.9		
23934624593497728	351.32675	-17.86607	GC	*	2.4	3.1	2.3	0.0	7.6	0.000	15.6	19.6	-1.1	DA [3]	23630	0.58	0.6	7.0		
648572418733377856	355.75224	-64.70386	GC	1	2.0	2.9	2.0	1.8	15.4	0.019	16.5	19.0	-0.7	DC [1]	5790	0.58	0.5	0.8		
2763719512462656000	356.55201	11.98061	GC	*	2.0	3.2	2.0	0.2	10.9	0.374	16.7	19.3	-0.8	DC [14]	6210	0.78	0.0	7.7		
6525205175564946816	356.55229	-47.24147	GC	*	1.4	2.1	2.0	0.7	16.3	0.458	15.5	19.0	-0.8	DA [5]	12500	0.64	0.0	7.7		

Note.—Description of columns: Legend for the Sample column: Ca II are objects with previously identified Ca II gas emission (Table 3). IR refers to non-Ca II debris disk systems (Table 4). CV are known cataclysmic variables, and GC are objects from our Gaia-cat-WISE crossmatch. Objects flagged with asterisks are believed to be newly discovered near-infrared variables; they are not known CVs nor are they published in Swan et al. (2019, 2020, 2021). We also flag known ZZ Ceti's [a] (Fontaine et al. 2003), [b] (Romero et al. 2022), [c] (Vauchair et al. 1997), [d] (Grannas et al. 2006), [e] (Vauchair et al. 1992), [f] (Kanaan et al. 2000), [g] (Vauchair et al. 2019), [h] (Romero et al. 2019), [i] (Vauclair et al. 1987). We define G<sub>RP</sub> Excess as the ratio of the summed flux in the Gaia RP bandpass in a 30° cone around the target white dwarf's RP flux. Flag legend: 1=contaminated as seen in WISE View, 2=false-positive variability due to a seasonal alternating pattern, 3=contaminated both as seen in WISE View and from altering S/N. W1 is the median signal-to-noise ratio of our W1 light curves. All magnitudes are reported here on the AB scale. catWISE View W1 – W2 colors are also on the AB scale. References for the tabulated spectral types are as follows: [1] O'Brien et al. (2024), [2] Coura et al. (2019), [3] McCook & Sion (1989), [4] Guo et al. (2015), [5] Vincent et al. (2005), [6] Koester et al. (2015), [7] Meinunger (1984), [8] Kilkenney et al. (1984), [9] Subasavage et al. (2022), [10] Grannas et al. (2021), [11] O'Brien et al. (2021), [12] Jimenez et al. (2021), [13] Deniley et al. (2013), [14] Kester et al. (1982), [15] Kester et al. (2015), [16] Limoges et al. (2020), [17] O'Donoghue et al. (2013), [18] Bateson et al. (2020), [19] Melis et al. (2020), [20] Gentile Fusillo et al. (2013), [21] Zhang et al. (2013), [22] Howarth (1978), [23] Kilic et al. (2020), [24] Warner (1974), [25] Udaliski (1990), [26] Radic et al. (2017), [27] Kleinman et al. (2017), [28] Sayres et al. (2012), [29] Simon et al. (2014), [30] Bergeron et al. (2001), [31] Caron et al. (2023), [32] Burbidge & Sritmatteer (1971), [33] Bergeron et al. (2019), [34] Tremblay et al. (2012), [35] Kawka & Vennes (2012), [36] Kilic et al. (2012), [37] McCleery et al. (2020), [38] Kato et al. (2000), [39] Bergeron et al. (2000), [40] Tremblay et al. (2011), [41] Harrison et al. (2009). T<sub>eff</sub> and M<sub>WD</sub> are derived from Gaia photometry assuming a hydrogen-dominated atmosphere (Gentile Fusillo et al. 2021b). EFF=EXCESSFLUX prior (Gentile Fusillo et al. 2021b). F<sub>oM</sub> is the Figure of Merit metric computed from the Gaia-AllWISE neighbor crossmatch analysis (Marrese et al. 2017, 2019, 2022). In the TESS column we report the significant periodicities in TBSS that we attributed intrinsic to the white dwarf using TESS-localize in hours and the associated amplitude in %.

**Table 3.** Variability Parameters for the 21 Published White Dwarf Debris Disks That Show Calcium II Gas in Emission

Figure 6	Gaia DR3 Source ID	Alt. Name	R.A. (J2000)	Decl. (J2000)	$\chi^2_{W1}$	$\chi^2_{\text{alt}}$	$\chi^2_{W2}$	S/N	$G_{\text{RP}}$ Excess	$G_{\text{RP}}$	W1 (mag)	W1 – W2 (mag)	$T_{\text{eff}}$ (K)	$M_{\text{WD}}$ ( $M_{\odot}$ )	EFF	FoM	
a	2860923998433585664	SDSS J0006+2858	1.64464	28.97960	1	0.3	0.3	1.0	5.3	237.861	16.5	18.1	-0.0	21980	0.55	1.7	
b	28105778-331734464	WD 0145+234	26.97841	23.66211	422.6	690.7	482.4	254.9	54.3	0.021	14.1	16.9	-0.4	12980	0.66	0.8	
c	2489275328645218560	SDSS J0234-0406	38.56461	-4.10258	1	1.2	1.8	1.3	0.6	12.5	3.039	16.5	-0.5	13100	0.63	0.7	
d	436298277884160	SDSS J0347+1624	56.90288	16.40270	*	12.3	17.7	12.1	0.5	11.2	0.940	16.7	-0.4	17710	0.52	0.0	
e	3415788525598117548	LAMOST J0510+2315	77.50894	23.26151	*	41.9	65.9	49.5	16.0	41.8	0.796	15.2	17.4	-0.1	21250	0.73	0.0
f	482304235496728832	WD J0523401	82.30968	-34.01892	*	2.0	2.2	6.4	0.8	28.5	0.230	17.6	18.4	0.1	17190	0.46	0.0
g	5279484614703730944	Gaia J06116931	92.88208	-69.51726	1	45.6	129.8	93.1	22.6	120.3	4.803	16.9	17.1	0.1	16140	0.54	0.0
h	3105360521513256832	Gaia J06440352	101.02179	-3.56845	1	2.2	2.9	2.2	2.1	7.6	25.020	16.3	19.2	0.0	17780	0.56	0.0
i	671450448046315520	SDSS J0734+1835	114.67736	18.58603	1	1.1	1.8	1.0	0.3	5.3	6.238	17.8	20.0	-0.3	15740	0.72	0.1
j	689352219629097856	WD 0842+231	131.41326	22.95785	1.7	2.4	1.7	1.7	1.7	22.8	0.000	16.0	18.3	-0.2	19180	0.58	0.0
k	1037258858615762048	WD 0842+72	131.51030	57.05705	*	25.2	37.1	26.1	9.0	95.4	0.090	16.9	16.4	0.0	15410	0.57	0.1
l	382959852857720832	SDSS J0955-0200	149.76957	-2.0.323	1.0	1.5	1.0	0.0	0.0	4.7	0.000	18.2	20.2	-0.0	11330	0.48	0.0
m	3869060540584643328	WD 1041+092	16.0.92305	8.93287	0.8	1.4	0.8	0.0	5.1	0.000	17.4	20.2	-1.0	16060	0.59	0.0	
n	390441578794792096	SDSS J1228+1040	18.7.24973	10.67585	1.5	2.2	2.0	1.3	15.8	0.122	16.6	18.8	-0.0	19310	0.62	0.4	
o	6287259310145684608	HB 1349-2305	208.18385	-23.33483	0.9	1.4	1.7	1.0	13.8	0.086	16.6	18.9	-0.4	16540	0.53	0.0	
p	4465269178854732160	SDSS J1617+1620	244.32100	16.33960	1.4	2.2	1.7	1.0	13.2	0.718	17.2	19.2	-0.4	13220	0.63	0.0	
q	1623866184737702912	WD 1622+87	245.74852	58.67525	*	9.8	14.8	9.2	2.9	20.9	0.152	17.0	19.2	-0.2	18790	0.48	1.5
r	66466388754073984	WD J19350528	292.65688	-50.47136	1.0	1.3	1.0	0.7	12.3	0.482	17.1	19.2	0.0	13570	0.63	0.9	
s	1827949408167403252	Gaia J2100+2122	315.14437	21.38247	2	6.7	6.2	6.7	1.9	53.8	1.772	15.4	17.3	0.0	25330	0.65	10.2
t	1797494081674032512	SDSS J2133+2428	323.46132	24.46831	1	12.9	23.5	15.1	4.2	17.2	1.536	17.5	18.9	-0.3	26320	0.58	0.0
u	2600209141285265280	ATLAS J22121352	333.01198	-13.87777	1	1.7	1.9	1.7	1.7	10.5	2.554	17.5	19.1	0.1	19360	0.53	0.0

NOTE—Description of columns: Flag: legend: 1=likely crowded ( $G_{\text{RP}}$  Excess  $> 1.415$ ), 2=likely alternating ( $\chi_{\text{alt}} < \chi_{W1}^2$ , see Section 3). Asterisks denote new near-infrared variables. We define  $G_{\text{RP}}$  Excess as the ratio of the summed flux in the Gaia  $RP$  bandpass in a  $30''$  cone around the target white dwarf to target white dwarf's  $RP$  flux (Section 3).  $S/N_{W1}$  is the median signal-to-noise ratio of our  $W1$  light curves. All magnitudes are reported here on the AB scale, catWISE  $W1 - W2$  colors are also on the AB scale.  $T_{\text{eff}}$  and  $M_{\text{WD}}$  are derived from Gaia photometry assuming a hydrogen-dominated atmosphere (Gentile Fusillo et al. 2021b). EFF=EXCESS\_FLUX\_ERROR (Gentile Fusillo et al. 2021b). FoM is the Figure of Merit metric computed from the Gaia-AllWISE neighbor crossmatch analysis (Marrese et al. 2017, 2019, 2022). We also guide the reader to Table 3 of Gentile Fusillo et al. (2021a) for a summary of the gaseous species in emission towards these 21 white dwarfs.

**Table 4.** Variability Parameters for the White Dwarf Debris Disks That Do Not Show Calcium II Gas in Emission

Figure 7, 8	Gaia DR3 Source ID	SIMBAD ID	R.A. (J2000)	Decl. (J2000)	Flag	$\chi^2_{W1}$	$\chi^2_{\text{alt}}$	$\chi^2_{\text{flat}}$	S/N	GRP Excess	GRP	W1 (mag)	W1 – W2 (mag)	$T_{\text{eff}}$ (K)	$M_{\text{WD}}$ ( $M_{\odot}$ )	EFF	FoM	
1	2859951106737135488	PG 0010+281	3.33780	28.33884	1.0	1.8	1.0	1.5	15.6	0.200	15.9	18.9	-0.5	25150	0.52	0.0	5.6	
2	502606346179493520	Ton S 193	17.15014	-32.62872	2.2	2.6	2.5	0.9	28.9	1.110	15.5	18.1	-0.7	16050	0.63	0.0		
3	491358920324379776	JL 234	18.08509	-56.24098	2.6	4.1	2.7	1.1	20.4	0.000	15.9	18.8	-0.3	18790	0.59	0.0	8.7	
4	95297185335197120	Wolf 88	27.23665	19.04097	2	5.2	4.3	4.9	1.8	0.022	15.5	18.0	0.0	11690	0.77	0.0	10.2	
5	251836059558271232	GALEX J01550.2+043131	28.95924	4.55216	1.5	2.2	1.4	5.7	0.000	16.9	20.0	-0.8	14110	0.55	0.0	6.0		
6	547501811501141248	EGGR 474	42.96365	73.69309	1	0.6	0.7	6.3	4.494	0.062	20.2	-0.6	8600	0.81	0.0	3.1		
7	5187830356195791488	GD 40	45.72127	-1.14227	1.2	1.7	1.2	1.3	22.2	0.000	15.5	18.4	-0.2	14090	0.60	0.0	9.1	
8	13611477105824	HS 0307+0746	47.53816	7.95891	1.1	1.6	1.0	0.0	8.3	0.000	16.1	19.5	-0.8	10100	0.59	0.6	8.4	
9	32517483151543296	GD 56	62.75904	-3.97294	4.9	6.8	40.0	3.3	56.2	0.268	15.7	17.1	0.2	14900	0.61	0.1	10.7	
10	4653404070862114176	MCT 0420-7310	64.90760	-73.06236	*	2.4	3.9	3.5	1.3	59.6	0.150	15.7	17.7	-0.1	17790	0.58	0.0	9.6
11	2711992114775824640	KPD 0420+5203	66.00547	52.16962	*	3.1	4.9	17.4	2.2	40.1	0.876	15.2	17.6	-0.3	22170	0.66	0.9	8.9
12	203311632475891184	GD 61	69.66406	41.51899	1	1.1	1.1	0.9	21.7	4.625	14.9	18.1	-0.5	16940	0.63	0.9		
13	706076062068973952	GALEX J084244.5+294815	130.68559	29.80441	0	0.0	4.0	4.0	13.083	18.5	20.4	-0.2	13120	0.47	0.0			
14	102908145283108480	PG 0843+517	131.75953	51.48149	0.9	1.5	0.9	0.6	17.9	0.000	16.3	18.9	-0.3	21210	0.51	0.2	7.4	
15	692795546450243456	GALEX J085028.3+271956	132.61811	27.33230	0.4	0.5	0.5	0.2	6.7	0.000	17.5	19.9	-0.6	18900	0.58	0.0	0.0	
16	719422660057614080	GALEX J09025.5+394339	136.35620	39.72756	0	0.7	0.9	0.7	0.0	0.269	18.0	0.1	12970	0.34	0.0			
17	618339424181751552	GALEX J092801.1+133219	142.00460	13.55869	0.7	0.9	0.7	0.0	4.5	0.000	18.1	20.3	0.1	22500	0.63	0.0	5.9	
18	3588723386196630784	PG 1015+161	154.51595	15.86627	0.8	1.0	0.8	1.0	18.6	0.032	15.8	18.6	-0.3	18370	0.60	0.0	7.4	
19	804169064957527552	PG 1031+411	155.48181	40.83747	1	1.4	2.2	1.4	0.2	8.7	4.317	16.6	19.6	-0.4	20740	0.63	0.0	8.0
20	336204030575124184	PG 1031+063	158.52221	6.04658	2	0.9	0.9	0.0	7.0	0.000	16.5	19.8	-1.0	19600	0.54	0.2	3.0	
21	3808488483665268736	GALEX J105807.8+020648	164.53280	2.11356	0	0.3	0.2	4.6	0.000	17.0	20.3	-0.1	17350	0.52	0.0	5.4		
22	3810933247769901696	GD 133	169.80166	2.34251	2	2.3	2.2	2.8	0.6	48.8	0.008	14.7	17.3	-0.2	12150	0.63	1.1	
23	401978959821201536	US 2966	176.99441	28.53223	*	1.9	3.1	2.6	0.9	10.1	0.245	17.5	19.4	0.1	11990	0.58	0.3	8.3
24	379641419249498880	LBQS US 1145+045	177.31358	-15.61014	4.6	6.6	4.3	3.2	40.5	0.000	17.3	20.1	-0.1	16030	0.66	5.4	6.8	
25	3571559292842744907	EC 11507-1519	185.46171	12.75370	1	1.0	1.7	1.0	0.4	8.7	1.687	18.3	19.5	-0.1	11770	0.62	0.1	9.4
26	3308649148333227232	GALEX J122450.8+124512	186.94733	-8.24388	1.8	2.1	1.7	2.0	28.4	0.030	14.7	18.0	-0.7	11720	0.77	0.0	8.4	
27	358318157126530656	PG 1255-079	188.63615	56.11195	1.9	2.5	1.8	0.5	8.7	0.258	18.1	19.8	-0.0	12570	0.70	13.2	7.2	
28	157158453980588544	SBSS 1232+563	190.63830	1.48317	0.3	0.5	0.4	0.4	5.2	0.000	17.3	20.1	-0.1	16030	0.66	5.4		
29	4011097017323921920	GALEX J1145-1045	178.31358	-15.61014	4.6	6.6	4.3	3.2	40.5	0.046	16.0	19.8	-1.0	12390	0.69	1.3		
30	118807543368561792	PG 1454-173	224.17141	17.07087	1.4	2.0	1.4	5.6	0.046	17.3	20.2	-0.2	11770	0.62	0.1			
31	1281989124433286912	EGGR 298	224.52704	29.62487	2	2.4	2.2	3.9	0.5	15.0	0.047	15.2	19.1	-0.2	7340	0.58	0.0	
32	63321729727430512	PG 1457-086	224.97079	-8.82490	2	1.3	1.2	1.4	0.4	10.9	0.014	15.9	19.2	-1.0	18330	0.51	2.1	6.6
33	12888122126531232	GALEX J150701.9+324545	226.75835	32.76250	3	1.4	1.4	0.7	6.4	1.864	18.5	20.2	-0.2	6960	0.53	0.1		
34	159529850182700960	SBSS 1536+520	234.35719	51.85745	0.5	1.1	0.5	3.8	0.000	18.9	20.8	-0.1	14820	0.86	0.0	2.6		
35	118807543368561792	PG 1454-173	224.17141	17.07087	1.4	2.0	1.4	5.6	0.047	17.3	20.2	-0.2	34150	0.76	0.0			
36	119653198854226560	KUV 1519+1730	235.43704	64.80805	2	2.4	2.2	3.9	0.5	15.0	0.044	15.2	19.1	-0.2	13210	0.59	0.0	
37	445459923843776128	GALEX J150720.8+091625	239.33658	9.27355	0	0.0	0.0	0.1	3.7	0.000	18.8	20.7	0.2	25260	0.51	1.6	3.3	
38	133644247212656000	GD 362	262.89299	37.08909	3	3.2	1.3	3.3	1.1	31.4	66.096	16.0	18.3	0.1	10480	0.70	0.0	10.2
39	428765495963143168	GALEX J193156.8+011745	292.98722	1.29559	3	0.5	0.4	0.5	0.6	28.2	5.375	14.5	16.8	-0.2	21540	0.62	0.7	
40	646291189717050240	LAWD 84	319.90222	-55.83735	2	24.8	1.6	23.3	1.6	50.7	0.062	14.2	17.3	-0.1	9520	0.58	0.0	10.1
41	174234278482615936	HS 21324-0941	323.71172	9.92229	0.8	1.2	0.8	1.2	0.6	12.2	0.054	16.0	19.2	-0.6	15630	0.58	0.0	
42	659231572319216896	L 570-26	325.48985	-33.00828	2	4.5	1.6	4.9	1.5	55.9	0.007	14.2	17.1	-0.6	7550	0.71	0.3	
43	26833717856030280	Gaia DR2 26832717856030280	331.01273	2.55887	1.2	1.7	1.1	0.1	6.5	0.000	17.3	19.9	-0.1	15480	0.67	0.8	2.6	
44	27270442757136760	GALEX J220394.8+122337	332.39521	12.39349	1.5	2.4	1.4	10.8	1.150	17.4	19.3	-0.1	14450	0.54	0.0			
45	239572828704350720	PHL 5103	336.07265	-16.26310	1.6	2.3	3.4	0.7	19.5	0.663	15.9	18.5	-0.4	9900	0.67	0.0	8.2	
46	2660358032257156736	G 29 -38	352.19849	5.24840	2	23.7	5.9	23.9	7.0	46.8	0.049	13.1	16.4	0.1	11520	0.63	8.2	11.5

**Table 4** *continued*

**Table 4** (*continued*)

Figure 7, 8	Gaia DR3 Source ID	SIMBAD ID	R.A. (J2000)	Decl. (J2000)	Flag (J2000)	$\chi^2_{W1}$	$\chi^2_{\text{alt}}$	$\chi^2_{\text{flat}}$	$\chi^2_{W2}$	S/N	$G_{RP}$	Excess	$G_{RP}$	$W1$	$W1 - W2$	$T_{\text{eff}}$	$M_{WD}$	EFF	FoM
47	276260508857836288	PG 2328+108	352.67362	11.03513	1.3	2.1	1.5	0.9	12.3	0.673	15.7	19.1	-0.8	17870	0.46	0.0	8.3		

Note—Description of columns: Flag legend: 1=likely crowded ( $G_{RP}$  Excess  $> 1.415$ ), 2=likely alternating ( $\chi^2_{\text{alt}} < \chi^2_{W1}$ , see Section 3), 3=both likely crowded and likely alternating, and 0=insufficient  $W1$  data to analyze. Asterisks denote new near-infrared variables. We define  $G_{RP}$  Excess as the ratio of the summed flux in the Gaia  $RP$  bandpass in a  $30''$  cone around the target white dwarf to target white dwarf's  $RP$  flux (Section 3).  $S/N_{W1}$  is the median signal-to-noise ratio of our  $W1$  light curves. All magnitudes are reported here on the AB scale.  $T_{\text{eff}}$  and  $M_{WD}$  are derived from the AB scale.  $T_{\text{eff}}$  and  $M_{WD}$  are derived from Gaia photometry assuming a hydrogen-dominated atmosphere (Gentile Fusillo et al. 2021b). EFF=EXCESS.FLUX.ERROR (Gentile Fusillo et al. 2021b). FoM is the Figure of Merit metric computed from the Gaia-AllWISE neighbor crossmatch analysis (Marrese et al. 2017, 2019, 2022).

## B. LDT+DEVENY AND SOAR+GOODMAN FOLLOW-UP SPECTROSCOPY

Table 5 shows an observing log of all of the near-infrared spectra we publish in Figure 5. A description of our observing setups is found in Section 2.3.

**Table 5.** Log of Observations at LDT and SOAR

Gaia DR3 ID	WDJ Name	Instrument+Facility	UTC Date	$G_{RP}$	Exp. Time	S/N	Spectral Type	Ca II Detected?
				(mag)	(sec.)			
4907742035447425024	WD J0058–5638	SOAR+Goodman	2023-08-13	16.9	7200	38.5	DZ [1]	Absorption
5078074837769743744	WD J0302–2301	SOAR+Goodman	2023-08-13	15.9	5400	61.5	DA [2]	No
276192136878054656	WD J0406+5431	LDT+DeVeny	2024-02-05	15.5	7200	32.9	DA [2]	No
4653404070862114176	WD J0419–7303	SOAR+Goodman	2023-08-13	15.7	1800	38.9	DA [2]	No
271992414775824640	WD J0424+5210	LDT+DeVeny	2023-10-06	15.2	7200	47.6	DA [2]	No
720353602808918016	WD J0857+4016	LDT+DeVeny	2024-02-05	15.0	7200	35.4	DA [2]	No
6306842338087328512	WD J1500–1603	SOAR+Goodman	2023-08-18	16.9	6600	21.7	DA [1]	No

NOTE—We calculate the tabulated signal-to-noise ratios (S/N) by taking the average of the ratio of the continuum normalized flux to its standard deviation at the wavelengths where we do not see features from the calcium triplet. References for the tabulated spectral types are as follows: [1] Vincent et al. (2024), [2] McCook & Sion (1999).

## C. LIGHT CURVES

Here we show our light curves of all 21 published Ca II gas disks in our original input in Figure 6. We show the first half of the 47 non-Ca II disks in Figure 7 and the second half in Figure 8.

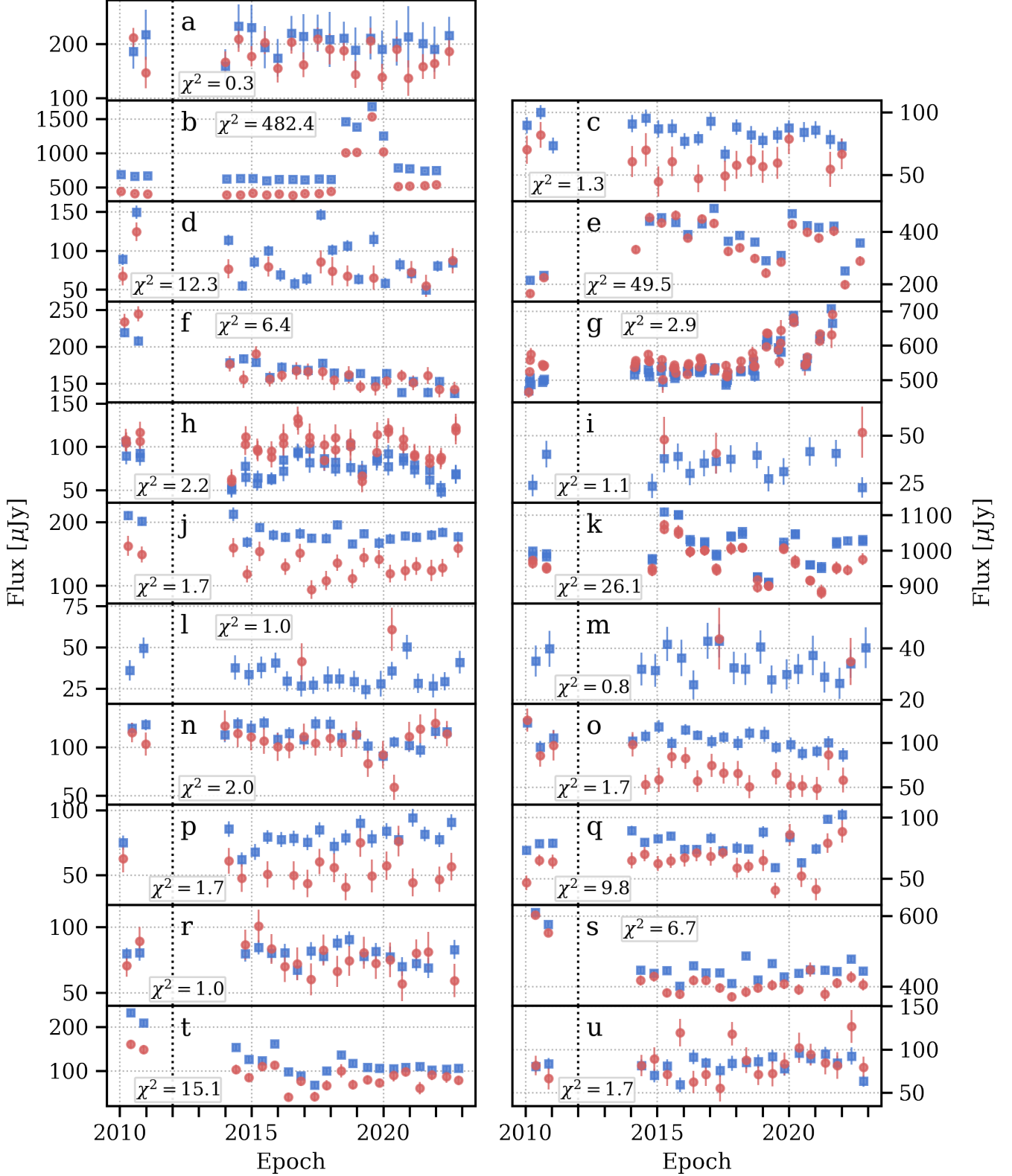


**Figure 6.** Our WISE light curves for all 21 published white dwarfs known to harbor Ca II gas disks (Gentile Fusillo et al. 2021a), plotted following the convention in Figure 1. Objects are shown in ascending order of right ascension. See Table 3 for full information on this sub-sample.

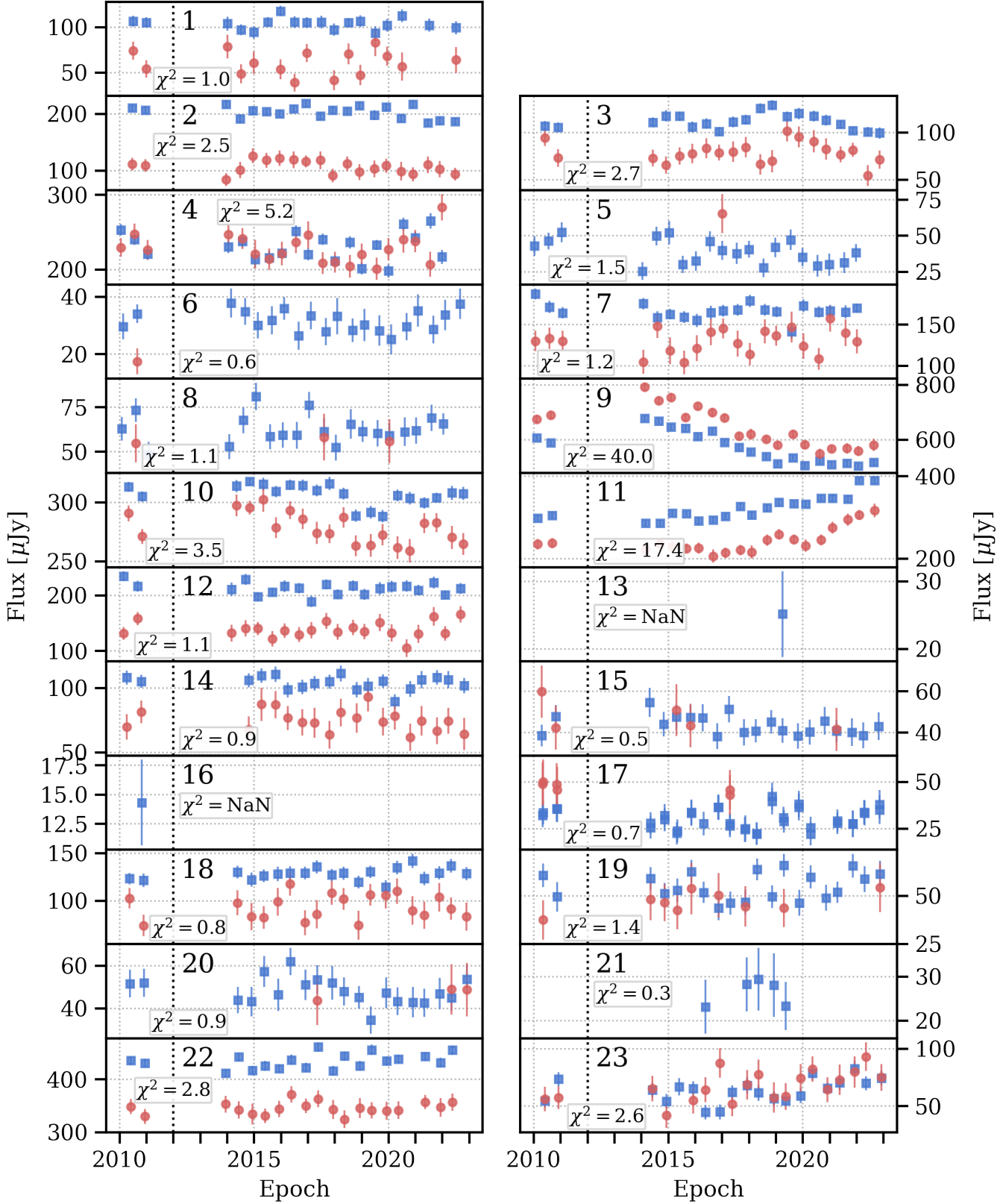


**Figure 7.** Our WISE light curves for the first 23 of the non-Ca II disk systems included in our input catalog, plotted following the convention in Figure 1. Objects are shown in ascending order of right ascension. See Table 4 for full information on this sub-sample.

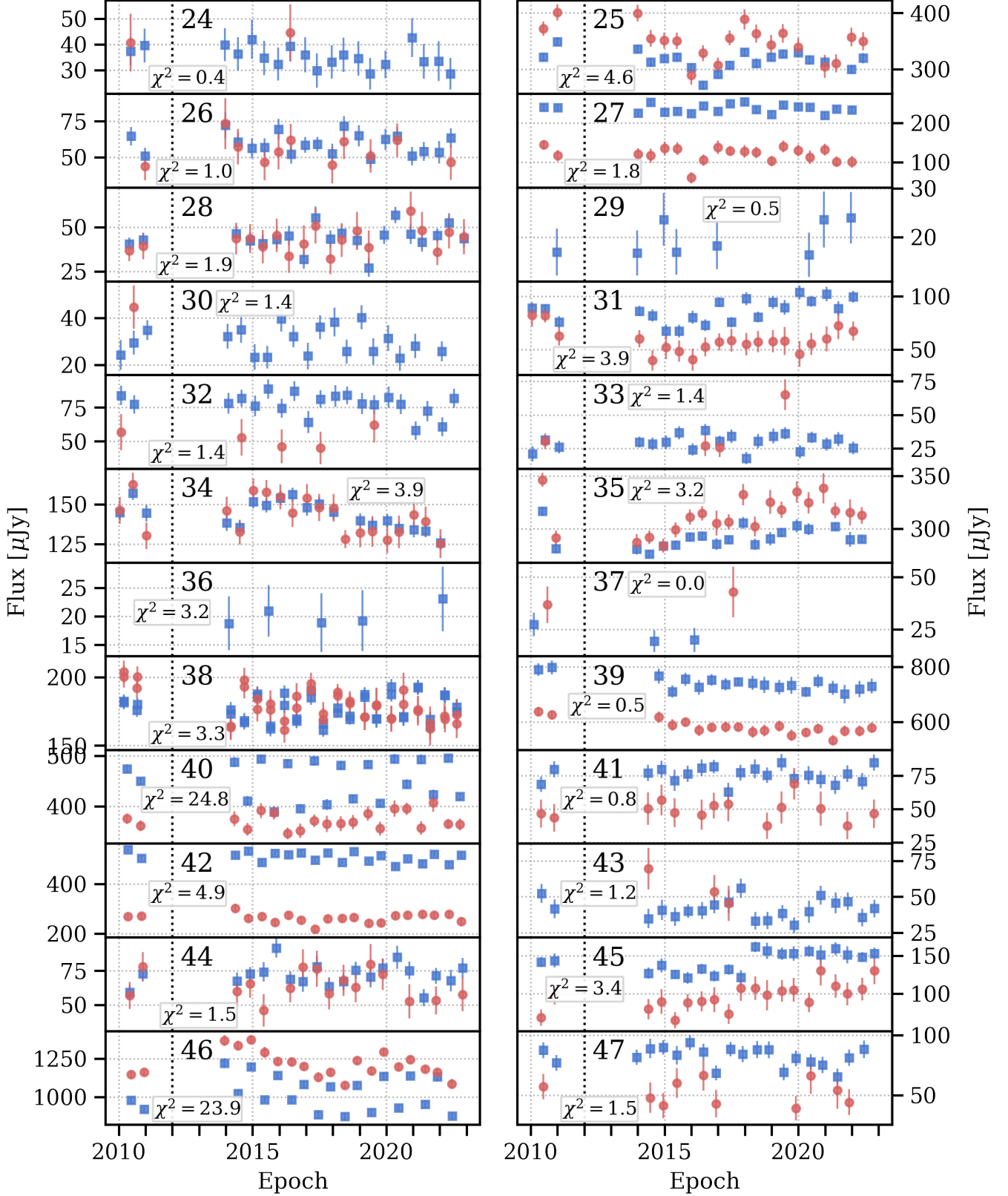


**Figure 8.** Continuation of Figure 7, showing the remaining 24 non-Ca II disks. These light curves are plotted following the convention in Figure 1. Objects are shown in ascending order of right ascension. See Table 4 for full information on this sub-sample.

## REFERENCES

- Astropy Collaboration, Robitaille, T. P., Tollerud, E. J., et al. 2013, A&A, 558, A33, doi: [10.1051/0004-6361/201322068](https://doi.org/10.1051/0004-6361/201322068)
- Astropy Collaboration, Price-Whelan, A. M., Sipőcz, B. M., et al. 2018, AJ, 156, 123, doi: [10.3847/1538-3881/aabc4f](https://doi.org/10.3847/1538-3881/aabc4f)
- Barber, S. D., Belardi, C., Kilic, M., & Gianninas, A. 2016, MNRAS, 459, 1415, doi: [10.1093/mnras/stw683](https://doi.org/10.1093/mnras/stw683)
- Bateson, F. M., McIntosh, R., & Brunt, D. 1991, Royal Astronomical Society of New Zealand Publications of Variable Star Section, 17, 38
- Bergeron, P., Leggett, S. K., & Ruiz, M. T. 2001, ApJS, 133, 413, doi: [10.1086/320356](https://doi.org/10.1086/320356)
- Bergeron, P., Ruiz, M. T., & Leggett, S. K. 1997, ApJS, 108, 339, doi: [10.1086/312955](https://doi.org/10.1086/312955)
- Bergeron, P., Wesemael, F., Dufour, P., et al. 2011, ApJ, 737, 28, doi: [10.1088/0004-637X/737/1/28](https://doi.org/10.1088/0004-637X/737/1/28)
- Bergeron, P., Wesemael, F., Fontaine, G., et al. 2021, AJ, 162, 188, doi: [10.3847/1538-3881/ac22b1](https://doi.org/10.3847/1538-3881/ac22b1)
- Bida, T. A., Dunham, E. W., Massey, P., & Roe, H. G. 2014, in Society of Photo-Optical Instrumentation Engineers (SPIE) Conference Series, Vol. 9147, Ground-based and Airborne Instrumentation for Astronomy V, ed. S. K. Ramsay, I. S. McLean, & H. Takami, 91472N, doi: [10.1117/12.2056872](https://doi.org/10.1117/12.2056872)
- Brinkworth, C. S., Marsh, T. R., Morales-Rueda, L., et al. 2005, MNRAS, 357, 333, doi: [10.1111/j.1365-2966.2005.08649.x](https://doi.org/10.1111/j.1365-2966.2005.08649.x)
- Brouwers, M. G., Bonsor, A., & Malamud, U. 2022, MNRAS, 509, 2404, doi: [10.1093/mnras/stab3009](https://doi.org/10.1093/mnras/stab3009)
- Burbidge, E. M., & Strittmatter, P. A. 1971, ApJL, 170, L39, doi: [10.1086/180836](https://doi.org/10.1086/180836)
- Caron, A., Bergeron, P., Blouin, S., & Leggett, S. K. 2023, MNRAS, 519, 4529, doi: [10.1093/mnras/stac3733](https://doi.org/10.1093/mnras/stac3733)
- Clemens, J. C., Crain, J. A., & Anderson, R. 2004, in Society of Photo-Optical Instrumentation Engineers (SPIE) Conference Series, Vol. 5492, Ground-based Instrumentation for Astronomy, ed. A. F. M. Moorwood & M. Iye, 331–340, doi: [10.1117/12.550069](https://doi.org/10.1117/12.550069)
- Coutu, S., Dufour, P., Bergeron, P., et al. 2019, ApJ, 885, 74, doi: [10.3847/1538-4357/ab46b9](https://doi.org/10.3847/1538-4357/ab46b9)
- Debes, J. H., Kilic, M., Faedi, F., et al. 2012, ApJ, 754, 59, doi: [10.1088/0004-637X/754/1/59](https://doi.org/10.1088/0004-637X/754/1/59)
- Dennihy, E., Clemens, J. C., Debes, J. H., et al. 2017, ApJ, 849, 77, doi: [10.3847/1538-4357/aa8ef2](https://doi.org/10.3847/1538-4357/aa8ef2)
- Dennihy, E., Clemens, J. C., Dunlap, B. H., et al. 2018, ApJ, 854, 40, doi: [10.3847/1538-4357/aaa89b](https://doi.org/10.3847/1538-4357/aaa89b)
- Dennihy, E., Farihi, J., Gentile Fusillo, N. P., & Debes, J. H. 2020a, ApJ, 891, 97, doi: [10.3847/1538-4357/ab7249](https://doi.org/10.3847/1538-4357/ab7249)
- Dennihy, E., Xu, S., Lai, S., et al. 2020b, ApJ, 905, 5, doi: [10.3847/1538-4357/abc339](https://doi.org/10.3847/1538-4357/abc339)
- Dominik, C., & Decin, G. 2003, ApJ, 598, 626, doi: [10.1086/379169](https://doi.org/10.1086/379169)
- Doré, O., Werner, M. W., Ashby, M. L. N., et al. 2018, arXiv e-prints, arXiv:1805.05489, doi: [10.48550/arXiv.1805.05489](https://doi.org/10.48550/arXiv.1805.05489)
- Dufour, P., Blouin, S., Coutu, S., et al. 2017, in Astronomical Society of the Pacific Conference Series, Vol. 509, 20th European White Dwarf Workshop, ed. P. E. Tremblay, B. Gaensicke, & T. Marsh, 3, <https://arxiv.org/abs/1610.00986>
- Eisenhardt, P. R. M., Marocco, F., Fowler, J. W., et al. 2020, ApJS, 247, 69, doi: [10.3847/1538-4365/ab7f2a](https://doi.org/10.3847/1538-4365/ab7f2a)
- Eyer, L., Audard, M., Holl, B., et al. 2023, A&A, 674, A13, doi: [10.1051/0004-6361/202244242](https://doi.org/10.1051/0004-6361/202244242)
- Farihi, J. 2016, NewAR, 71, 9, doi: [10.1016/j.newar.2016.03.001](https://doi.org/10.1016/j.newar.2016.03.001)
- Farihi, J., Becklin, E. E., & Zuckerman, B. 2005, ApJS, 161, 394, doi: [10.1086/444362](https://doi.org/10.1086/444362)
- Farihi, J., Gänsicke, B. T., Steele, P. R., et al. 2012, MNRAS, 421, 1635, doi: [10.1111/j.1365-2966.2012.20421.x](https://doi.org/10.1111/j.1365-2966.2012.20421.x)
- Farihi, J., van Lieshout, R., Cauley, P. W., et al. 2018, MNRAS, 481, 2601, doi: [10.1093/mnras/sty2331](https://doi.org/10.1093/mnras/sty2331)
- Fontaine, G., Bergeron, P., Billères, M., & Charpinet, S. 2003, ApJ, 591, 1184, doi: [10.1086/375490](https://doi.org/10.1086/375490)
- Gänsicke, B. T. 2011, in AIP Conf. Proc. 1331, Planetary Systems Beyond the Main Sequence, ed. S. Schuh, H. Drechsel, & U. Heber (Melville, NY: AIP), 211
- Gänsicke, B. T., Koester, D., Marsh, T. R., Rebassa-Mansergas, A., & Southworth, J. 2008, MNRAS, 391, L103, doi: [10.1111/j.1745-3933.2008.00565.x](https://doi.org/10.1111/j.1745-3933.2008.00565.x)
- Gänsicke, B. T., Marsh, T. R., & Southworth, J. 2007, MNRAS, 380, L35, doi: [10.1111/j.1745-3933.2007.00343.x](https://doi.org/10.1111/j.1745-3933.2007.00343.x)
- Gänsicke, B. T., Marsh, T. R., Southworth, J., & Rebassa-Mansergas, A. 2006, Science, 314, 1908, doi: [10.1126/science.1135033](https://doi.org/10.1126/science.1135033)
- Gänsicke, B. T., Schreiber, M. R., Toloza, O., et al. 2019, Nature, 576, 61, doi: [10.1038/s41586-019-1789-8](https://doi.org/10.1038/s41586-019-1789-8)
- Gentile Fusillo, N. P., Manser, C. J., Gänsicke, B. T., et al. 2021a, MNRAS, 504, 2707, doi: [10.1093/mnras/stab992](https://doi.org/10.1093/mnras/stab992)
- Gentile Fusillo, N. P., Tremblay, P. E., Cukanovaite, E., et al. 2021b, MNRAS, 508, 3877, doi: [10.1093/mnras/stab2672](https://doi.org/10.1093/mnras/stab2672)
- Gianninas, A., Bergeron, P., & Fontaine, G. 2006, AJ, 132, 831, doi: [10.1086/506516](https://doi.org/10.1086/506516)
- Gianninas, A., Bergeron, P., & Ruiz, M. T. 2011, ApJ, 743, 138, doi: [10.1088/0004-637X/743/2/138](https://doi.org/10.1088/0004-637X/743/2/138)

- Ginsburg, A., Sipócz, B. M., Brasseur, C. E., et al. 2019, AJ, 157, 98, doi: [10.3847/1538-3881/aafc33](https://doi.org/10.3847/1538-3881/aafc33)
- Girven, J., Gänsicke, B. T., Steeghs, D., & Koester, D. 2011, MNRAS, 417, 1210, doi: [10.1111/j.1365-2966.2011.19337.x](https://doi.org/10.1111/j.1365-2966.2011.19337.x)
- Guidry, J. A., Vanderbosch, Z. P., Hermes, J. J., et al. 2021, The Astrophysical Journal, 912, 125, doi: [10.3847/1538-4357/abee68](https://doi.org/10.3847/1538-4357/abee68)
- Guo, J., Zhao, J., Tziartzis, A., et al. 2015, MNRAS, 454, 2787, doi: [10.1093/mnras/stv2104](https://doi.org/10.1093/mnras/stv2104)
- Harris, C. R., Millman, K. J., van der Walt, S. J., et al. 2020, Nature, 585, 357, doi: [10.1038/s41586-020-2649-2](https://doi.org/10.1038/s41586-020-2649-2)
- Harrison, T. E., Bornak, J., Howell, S. B., et al. 2009, AJ, 137, 4061, doi: [10.1088/0004-6256/137/4/4061](https://doi.org/10.1088/0004-6256/137/4/4061)
- Hart, K., Shappee, B. J., Hey, D., et al. 2023, arXiv e-prints, arXiv:2304.03791, doi: [10.48550/arXiv.2304.03791](https://doi.org/10.48550/arXiv.2304.03791)
- Higgins, M. E., & Bell, K. J. 2023, AJ, 165, 141, doi: [10.3847/1538-3881/acb20c](https://doi.org/10.3847/1538-3881/acb20c)
- Hoard, D. W., Debes, J. H., Wachter, S., Leisawitz, D. T., & Cohen, M. 2013, ApJ, 770, 21, doi: [10.1088/0004-637X/770/1/21](https://doi.org/10.1088/0004-637X/770/1/21)
- Howarth, I. D. 1978, Journal of the British Astronomical Association, 88, 292
- Hunter, J. D. 2007, Computing in Science & Engineering, 9, 90, doi: [10.1109/MCSE.2007.55](https://doi.org/10.1109/MCSE.2007.55)
- Jarrett, T. H., Cohen, M., Masci, F., et al. 2011, ApJ, 735, 112, doi: [10.1088/0004-637X/735/2/112](https://doi.org/10.1088/0004-637X/735/2/112)
- Jura, M. 2003, ApJL, 584, L91, doi: [10.1086/374036](https://doi.org/10.1086/374036)
- Kanaan, A., Kepler, S. O., Giovannini, O., & Diaz, M. 1992, ApJL, 390, L89, doi: [10.1086/186379](https://doi.org/10.1086/186379)
- Kato, T., Hanson, G., Poyner, G., et al. 2000, Information Bulletin on Variable Stars, 4932, 1
- Kawka, A., & Vennes, S. 2012, MNRAS, 425, 1394, doi: [10.1111/j.1365-2966.2012.21574.x](https://doi.org/10.1111/j.1365-2966.2012.21574.x)
- Kilic, M., Bergeron, P., Kosakowski, A., et al. 2020, ApJ, 898, 84, doi: [10.3847/1538-4357/ab9b8d](https://doi.org/10.3847/1538-4357/ab9b8d)
- Kilic, M., Patterson, A. J., Barber, S., Leggett, S. K., & Dufour, P. 2012, MNRAS, 419, L59, doi: [10.1111/j.1745-3933.2011.01177.x](https://doi.org/10.1111/j.1745-3933.2011.01177.x)
- Kilkenny, D., Worters, H. L., O'Donoghue, D., et al. 2016, MNRAS, 459, 4343, doi: [10.1093/mnras/stw916](https://doi.org/10.1093/mnras/stw916)
- Kleinman, S. J., Kepler, S. O., Koester, D., et al. 2013, ApJS, 204, 5, doi: [10.1088/0067-0049/204/1/5](https://doi.org/10.1088/0067-0049/204/1/5)
- Kochanek, C. S., Shappee, B. J., Stanek, K. Z., et al. 2017, PASP, 129, 104502, doi: [10.1088/1538-3873/aa80d9](https://doi.org/10.1088/1538-3873/aa80d9)
- Koester, D., Gänsicke, B. T., & Farihi, J. 2014, A&A, 566, A34, doi: [10.1051/0004-6361/201423691](https://doi.org/10.1051/0004-6361/201423691)
- Koester, D., Rollenhagen, K., Napiwotzki, R., et al. 2005, A&A, 432, 1025, doi: [10.1051/0004-6361:20041927](https://doi.org/10.1051/0004-6361:20041927)
- Koester, D., Weidemann, V., & Zeidler, E. M. 1982, A&A, 116, 147
- Lang, D. 2014, AJ, 147, 108, doi: [10.1088/0004-6256/147/5/108](https://doi.org/10.1088/0004-6256/147/5/108)
- Limoges, M. M., Bergeron, P., & Lépine, S. 2015, ApJS, 219, 19, doi: [10.1088/0067-0049/219/2/19](https://doi.org/10.1088/0067-0049/219/2/19)
- Limoges, M. M., Lépine, S., & Bergeron, P. 2013, AJ, 145, 136, doi: [10.1088/0004-6256/145/5/136](https://doi.org/10.1088/0004-6256/145/5/136)
- Mainzer, A., Bauer, J., Grav, T., et al. 2011, ApJ, 731, 53, doi: [10.1088/0004-637X/731/1/53](https://doi.org/10.1088/0004-637X/731/1/53)
- Mainzer, A., Bauer, J., Cutri, R. M., et al. 2014, ApJ, 792, 30, doi: [10.1088/0004-637X/792/1/30](https://doi.org/10.1088/0004-637X/792/1/30)
- Mainzer, A. K., Masiero, J. R., Abell, P. A., et al. 2023, PSJ, 4, 224, doi: [10.3847/PSJ/ad0468](https://doi.org/10.3847/PSJ/ad0468)
- Malamud, U., Grishin, E., & Brouwers, M. 2021, MNRAS, 501, 3806, doi: [10.1093/mnras/staa3940](https://doi.org/10.1093/mnras/staa3940)
- Manser, C. J., Gänsicke, B. T., Gentile Fusillo, N. P., et al. 2020, MNRAS, 493, 2127, doi: [10.1093/mnras/staa359](https://doi.org/10.1093/mnras/staa359)
- Marrese, P. M., Marinoni, S., Fabrizio, M., & Altavilla, G. 2019, A&A, 621, A144, doi: [10.1051/0004-6361/201834142](https://doi.org/10.1051/0004-6361/201834142)
- . 2022, Gaia DR3 documentation Chapter 15: Cross-match with external catalogues, Gaia DR3 documentation, European Space Agency; Gaia Data Processing and Analysis Consortium.
- Marrese, P. M., Marinoni, S., Fabrizio, M., & Giuffrida, G. 2017, A&A, 607, A105, doi: [10.1051/0004-6361/201730965](https://doi.org/10.1051/0004-6361/201730965)
- Masterson, M., De, K., Panagiotou, C., et al. 2024, ApJ, 961, 211, doi: [10.3847/1538-4357/ad18bb](https://doi.org/10.3847/1538-4357/ad18bb)
- McCleery, J., Tremblay, P.-E., Gentile Fusillo, N. P., et al. 2020, MNRAS, 499, 1890, doi: [10.1093/mnras/staa2030](https://doi.org/10.1093/mnras/staa2030)
- McCook, G. P., & Sion, E. M. 1999, ApJS, 121, 1, doi: [10.1086/313186](https://doi.org/10.1086/313186)
- Meinunger, L. 1984, Information Bulletin on Variable Stars, 2483, 1
- Meisner, A. M., Caselden, D., Schlafly, E. F., & Kiwy, F. 2023, AJ, 165, 36, doi: [10.3847/1538-3881/aca2ab](https://doi.org/10.3847/1538-3881/aca2ab)
- Meisner, A. M., Lang, D., Schlafly, E. F., & Schlegel, D. J. 2019, PASP, 131, 124504, doi: [10.1088/1538-3873/ab3df4](https://doi.org/10.1088/1538-3873/ab3df4)
- Meisner, A. M., Lang, D., & Schlegel, D. J. 2017a, AJ, 153, 38, doi: [10.3847/1538-3881/153/1/38](https://doi.org/10.3847/1538-3881/153/1/38)
- . 2017b, AJ, 154, 161, doi: [10.3847/1538-3881/aa894e](https://doi.org/10.3847/1538-3881/aa894e)
- Meisner, A. M., Lang, D. A., & Schlegel, D. J. 2018, Research Notes of the American Astronomical Society, 2, 202, doi: [10.3847/2515-5172/aaecd5](https://doi.org/10.3847/2515-5172/aaecd5)
- Melis, C., Klein, B., Doyle, A. E., et al. 2020, ApJ, 905, 56, doi: [10.3847/1538-4357/abbdfa](https://doi.org/10.3847/1538-4357/abbdfa)
- Melis, C., Dufour, P., Farihi, J., et al. 2012, ApJL, 751, L4, doi: [10.1088/2041-8205/751/1/L4](https://doi.org/10.1088/2041-8205/751/1/L4)

- Nather, R. E., Robinson, E. L., & Stover, R. J. 1981, ApJ, 244, 269, doi: [10.1086/158704](https://doi.org/10.1086/158704)
- Newville, M., Stensitzki, T., Allen, D. B., & Ingargiola, A. 2014, LMFIT: Non-Linear Least-Square Minimization and Curve-Fitting for Python, 0.8.0, Zenodo, doi: [10.5281/zenodo.11813](https://doi.org/10.5281/zenodo.11813)
- O'Brien, M. W., Tremblay, P. E., Gentile Fusillo, N. P., et al. 2023, MNRAS, 518, 3055, doi: [10.1093/mnras/stac3303](https://doi.org/10.1093/mnras/stac3303)
- O'Brien, M. W., Tremblay, P. E., Klein, B. L., et al. 2024, MNRAS, 527, 8687, doi: [10.1093/mnras/stad3773](https://doi.org/10.1093/mnras/stad3773)
- O'Donoghue, D., Kilkenny, D., Koen, C., et al. 2013, MNRAS, 431, 240, doi: [10.1093/mnras/stt158](https://doi.org/10.1093/mnras/stt158)
- Ould Rouis, L. B., Hermes, J., & Gaensicke, B. 2024, in AAS/Division for Extreme Solar Systems Abstracts, Vol. 56, AAS/Division for Extreme Solar Systems Abstracts, 612.02
- pandas development team, T. 2020, pandas-dev/pandas: Pandas, latest, Zenodo, doi: [10.5281/zenodo.3509134](https://doi.org/10.5281/zenodo.3509134)
- Petrosky, E., Hwang, H.-C., Zakamska, N. L., Chandra, V., & Hill, M. J. 2021, MNRAS, 503, 3975, doi: [10.1093/mnras/stab592](https://doi.org/10.1093/mnras/stab592)
- Prochaska, J., Hennawi, J., Westfall, K., et al. 2020, The Journal of Open Source Software, 5, 2308, doi: [10.21105/joss.02308](https://doi.org/10.21105/joss.02308)
- Prša, A., Kochoska, A., Conroy, K. E., et al. 2022, ApJS, 258, 16, doi: [10.3847/1538-4365/ac324a](https://doi.org/10.3847/1538-4365/ac324a)
- Raddi, R., Gentile Fusillo, N. P., Pala, A. F., et al. 2017, MNRAS, 472, 4173, doi: [10.1093/mnras/stx2243](https://doi.org/10.1093/mnras/stx2243)
- Rebassa-Mansergas, A., Solano, E., Xu, S., et al. 2019, MNRAS, 489, 3990, doi: [10.1093/mnras/stz2423](https://doi.org/10.1093/mnras/stz2423)
- Ricker, G. R., Winn, J. N., Vanderspek, R., et al. 2015, Journal of Astronomical Telescopes, Instruments, and Systems, 1, 014003, doi: [10.1117/1.JATIS.1.1.014003](https://doi.org/10.1117/1.JATIS.1.1.014003)
- Rocchetto, M., Farihi, J., Gännsicke, B. T., & Bergfors, C. 2015, MNRAS, 449, 574, doi: [10.1093/mnras/stv282](https://doi.org/10.1093/mnras/stv282)
- Rodriguez, A. C., Kulkarni, S. R., Prince, T. A., et al. 2023a, ApJ, 945, 141, doi: [10.3847/1538-4357/acbb6f](https://doi.org/10.3847/1538-4357/acbb6f)
- Rodriguez, A. C., Galiullin, I., Gilfanov, M., et al. 2023b, ApJ, 954, 63, doi: [10.3847/1538-4357/ace698](https://doi.org/10.3847/1538-4357/ace698)
- Rogers, L. K., Xu, S., Bonsor, A., et al. 2020, MNRAS, 494, 2861, doi: [10.1093/mnras/staa873](https://doi.org/10.1093/mnras/staa873)
- Rogers, L. K., Bonsor, A., Xu, S., et al. 2024a, MNRAS, 527, 6038, doi: [10.1093/mnras/stad3557](https://doi.org/10.1093/mnras/stad3557)
- . 2024b, arXiv e-prints, arXiv:2406.11470. <https://arxiv.org/abs/2406.11470>
- Romero, A. D., Amaral, L. A., Klippen, T., et al. 2019, MNRAS, 490, 1803, doi: [10.1093/mnras/stz2571](https://doi.org/10.1093/mnras/stz2571)
- Romero, A. D., Kepler, S. O., Hermes, J. J., et al. 2022, MNRAS, 511, 1574, doi: [10.1093/mnras/stac093](https://doi.org/10.1093/mnras/stac093)
- Sayres, C., Subasavage, J. P., Bergeron, P., et al. 2012, AJ, 143, 103, doi: [10.1088/0004-6256/143/4/103](https://doi.org/10.1088/0004-6256/143/4/103)
- Schlafly, E. F., Meisner, A. M., & Green, G. M. 2019, ApJS, 240, 30, doi: [10.3847/1538-4365/aafbea](https://doi.org/10.3847/1538-4365/aafbea)
- Shappee, B. J., Prieto, J. L., Grupe, D., et al. 2014, ApJ, 788, 48, doi: [10.1088/0004-637X/788/1/48](https://doi.org/10.1088/0004-637X/788/1/48)
- Sion, E. M., Holberg, J. B., Oswalt, T. D., et al. 2014, AJ, 147, 129, doi: [10.1088/0004-6256/147/6/129](https://doi.org/10.1088/0004-6256/147/6/129)
- Steele, A., Debes, J., Xu, S., Yeh, S., & Dufour, P. 2021, ApJ, 911, 25, doi: [10.3847/1538-4357/abc262](https://doi.org/10.3847/1538-4357/abc262)
- Subasavage, J., Bergeron, P., Lépine, S., & Blouin, S. 2022, Montreal White Dwarf Database
- Swan, A., Farihi, J., Su, K. Y. L., & Desch, S. J. 2024, MNRAS, 529, L41, doi: [10.1093/mnrasl/slad198](https://doi.org/10.1093/mnrasl/slad198)
- Swan, A., Farihi, J., & Wilson, T. G. 2019, MNRAS, 484, L109, doi: [10.1093/mnras/slz014](https://doi.org/10.1093/mnras/slz014)
- Swan, A., Farihi, J., Wilson, T. G., & Parsons, S. G. 2020, MNRAS, 496, 5233, doi: [10.1093/mnras/staa1688](https://doi.org/10.1093/mnras/staa1688)
- Swan, A., Kenyon, S. J., Farihi, J., et al. 2021, MNRAS, 506, 432, doi: [10.1093/mnras/stab1738](https://doi.org/10.1093/mnras/stab1738)
- Taylor, M. B. 2005, in Astronomical Society of the Pacific Conference Series, Vol. 347, Astronomical Data Analysis Software and Systems XIV, ed. P. Shopbell, M. Britton, & R. Ebert, 29
- Tran, V., De, K., & Hillenbrand, L. 2024, MNRAS, doi: [10.1093/mnras/stae953](https://doi.org/10.1093/mnras/stae953)
- Tremblay, P. E., Hollands, M. A., Gentile Fusillo, N. P., et al. 2020, MNRAS, 497, 130, doi: [10.1093/mnras/staa1892](https://doi.org/10.1093/mnras/staa1892)
- Udalski, A. 1990, AJ, 100, 226, doi: [10.1086/115508](https://doi.org/10.1086/115508)
- Valyavin, G., Antonyuk, K., Plachinda, S., et al. 2011, ApJ, 734, 17, doi: [10.1088/0004-637X/734/1/17](https://doi.org/10.1088/0004-637X/734/1/17)
- Vauclair, G., Chevreton, M., & Dolez, N. 1987, A&A, 175, L13
- Vauclair, G., Dolez, N., Fu, J. N., & Chevreton, M. 1997, A&A, 322, 155
- Vauclair, G., Dolez, N., Fu, J. N., et al. 2000, Baltic Astronomy, 9, 133, doi: [10.1515/astro-2000-0120](https://doi.org/10.1515/astro-2000-0120)
- Veras, D. 2021, in Oxford Research Encyclopedia of Planetary Science, 1, doi: [10.1093/acrefore/9780190647926.013.238](https://doi.org/10.1093/acrefore/9780190647926.013.238)
- Vincent, O., Barstow, M. A., Jordan, S., et al. 2024, A&A, 682, A5, doi: [10.1051/0004-6361/202347694](https://doi.org/10.1051/0004-6361/202347694)
- Vincent, O., Bergeron, P., & Lafrenière, D. 2020, AJ, 160, 252, doi: [10.3847/1538-3881/abbe20](https://doi.org/10.3847/1538-3881/abbe20)
- Virtanen, P., Gommers, R., Oliphant, T. E., et al. 2020, Nature Methods, 17, 261, doi: [10.1038/s41592-019-0686-2](https://doi.org/10.1038/s41592-019-0686-2)
- Šimon, V. 2000, A&A, 360, 627
- Wang, L., Zhang, X., Wang, J., et al. 2023, ApJ, 944, 23, doi: [10.3847/1538-4357/acaf5a](https://doi.org/10.3847/1538-4357/acaf5a)

- Wang, T.-g., Jiang, N., Ge, J., et al. 2019, ApJL, 886, L5,  
doi: [10.3847/2041-8213/ab53ed](https://doi.org/10.3847/2041-8213/ab53ed)
- Warner, B. 1974, MNRAS, 168, 235,  
doi: [10.1093/mnras/168.1.235](https://doi.org/10.1093/mnras/168.1.235)
- Waskom, M. L. 2021, Journal of Open Source Software, 6,  
3021, doi: [10.21105/joss.03021](https://doi.org/10.21105/joss.03021)
- Wilson, D. J., Gänsicke, B. T., Koester, D., et al. 2014,  
MNRAS, 445, 1878, doi: [10.1093/mnras/stu1876](https://doi.org/10.1093/mnras/stu1876)
- Wilson, T. G., Farihi, J., Gänsicke, B. T., & Swan, A. 2019,  
MNRAS, 487, 133, doi: [10.1093/mnras/stz1050](https://doi.org/10.1093/mnras/stz1050)
- Wright, E. L., Eisenhardt, P. R. M., Mainzer, A. K., et al.  
2010, AJ, 140, 1868, doi: [10.1088/0004-6256/140/6/1868](https://doi.org/10.1088/0004-6256/140/6/1868)
- Xu, S., & Bonsor, A. 2021, Elements, 17, 241,  
doi: [10.2138/gselements.17.4.241](https://doi.org/10.2138/gselements.17.4.241)
- Xu, S., & Jura, M. 2014, ApJL, 792, L39,  
doi: [10.1088/2041-8205/792/2/L39](https://doi.org/10.1088/2041-8205/792/2/L39)
- Xu, S., Jura, M., Dufour, P., & Zuckerman, B. 2016, ApJL,  
816, L22, doi: [10.3847/2041-8205/816/2/L22](https://doi.org/10.3847/2041-8205/816/2/L22)
- Xu, S., Jura, M., Koester, D., Klein, B., & Zuckerman, B.  
2014, ApJ, 783, 79, doi: [10.1088/0004-637X/783/2/79](https://doi.org/10.1088/0004-637X/783/2/79)
- Xu, S., Su, K. Y. L., Rogers, L. K., et al. 2018, ApJ, 866,  
108, doi: [10.3847/1538-4357/aadce](https://doi.org/10.3847/1538-4357/aadce)
- Zhang, Y.-Y., Deng, L.-C., Liu, C., et al. 2013, AJ, 146, 34,  
doi: [10.1088/0004-6256/146/2/34](https://doi.org/10.1088/0004-6256/146/2/34)
- Zuckerman, B., Koester, D., Reid, I. N., & Hünsch, M.  
2003, ApJ, 596, 477, doi: [10.1086/377492](https://doi.org/10.1086/377492)
- Zuckerman, B., Melis, C., Klein, B., Koester, D., & Jura, M.  
2010, ApJ, 722, 725, doi: [10.1088/0004-637X/722/1/725](https://doi.org/10.1088/0004-637X/722/1/725)